# Ionic basis for membrane potential resonance in neurons of the inferior olive

**Yoshiko Matsumoto-Makidono[1], Hisako Nakayama[1], Miwako Yamasaki[2], Taisuke Miyazaki[2], Kazuto Kobayashi[3], Masahiko Watanabe[2], Masanobu Kano[4], Kenji Sakimura[5], and Kouichi Hashimoto[1]**

[1]Department of Neurophysiology, Graduate School of Biomedical and Health Sciences, Hiroshima University, 1-2-3 Kasumi, Hiroshima 734-8551, Japan

[2]Department of Anatomy, Hokkaido University Graduate School of Medicine, Sapporo 060-8638, Japan

[3]Department of Molecular Genetics, Institute of Biomedical Sciences, Fukushima Medical University School of Medicine, Fukushima 960-1295, Japan.

[4]Department of Neurophysiology, Graduate School of Medicine, The University of Tokyo, Hongo, Tokyo 113-0033, Japan

[5]Department of Cellular Neurobiology, Brain Research Institute, Niigata University, Niigata 951-8585, Japan

**Contact:** Kouichi Hashimoto

E-mail: hashik@hiroshima-u.ac.jp

**Summary**

Some neurons have the ability to enhance output voltage to input current with a preferred frequency, which is called resonance and thought to be a basis for membrane potential oscillation. Although ion channels responsible for resonance have been reported, precise mechanisms remain poorly understood. We found that resonance was reduced but clearly present in inferior olivary neurons of Cav3.1 T-type voltage-dependent $Ca^{2+}$ channel knockout (KO) mice. Activation of Cav3.1 channels was strongly membrane potential-dependent, but less frequency-dependent. Residual resonance in Cav3.1 KO mice was abolished by a hyperpolarization-activated cyclic nucleotide-gated (HCN) channel blocker, ZD7288, and was partially suppressed by voltage-dependent $K^+$ channel blockers. Resonance was inhibited by ZD7288 in wild-type mice and impaired in HCN1 KO mice, suggesting that the HCN1 channel was essential for resonance. The ZD7288-sensitive current was nearly sinusoidal and strongly frequency-dependent. These results suggested that Cav3.1 and HCN1 channels act as amplifying and resonating conductances, respectively.

## Introduction

Membrane potential oscillation is thought to play crucial roles in the generation of neural rhythms that underlie various brain functions (Buzsaki, 2006; Hutcheon and Yarom, 2000; Llinas, 1988; Wang, 2010). It is proposed that the ability to generate subthreshold membrane potential oscillations (STOs) is attributable to electrical resonant properties of the neuronal membrane (Hutcheon and Yarom, 2000; Llinas, 1988). The magnitude of membrane voltage in response to sinusoidal current injection is strongly enhanced when frequency of the injected current is close to a specific frequency (the resonant frequency) (Erchova et al., 2004; Hutcheon and Yarom, 2000; Lampl and Yarom, 1997; Puil et al., 1986), which results from a frequency-dependent enhancement of membrane impedance. Enhanced impedance is caused by electrical resonance that occurs in circuits that are electrically equivalent to the parallel resonant circuit inherent to the plasma membrane (Erchova et al., 2004; Hutcheon and Yarom, 2000; Narayanan and Johnston, 2008; Puil et al., 1986). The resistor and capacitor depend on the passive membrane property, and the phenomenological inductor is thought to be mediated by voltage-dependent ion channels (Hutcheon and Yarom, 2000).

There are several ion channel candidates for resonance, such as T-type voltage-dependent $Ca^{2+}$ channels (T-type VDCCs), hyperpolarization-activated cyclic nucleotide-gated (HCN) channels, persistent $Na^{+}$ channels, and M-type voltage-dependent $K^{+}$ (Kv) channels (Hutcheon and Yarom, 2000; Wang, 2010). It has been proposed that these

channels can be classified into two groups (Hutcheon et al., 1996a; Hutcheon and Yarom, 2000). One group acts as resonating conductances that play a role as phenomenological inductors, and the other acts as amplifying conductances that potentiate resonating conductance activity. Classification of these channels is mostly based on whether a channel blocker can significantly shift the resonant frequency (Hutcheon et al., 1996a; Hutcheon and Yarom, 2000). However, the precise roles of candidate ion channels in resonance remain unclear. For example, theoretical analyses suggest that T-type VDCCs have the potential to act as a resonating conductance (Hutcheon et al., 1994; Hutcheon and Yarom, 2000). However, the resonant frequency is not affected by the appropriate blockers in some studies (Gutfreund et al., 1995; Strohmann et al., 1994; Ulrich, 2014), suggesting that T-type VDCCs act as an amplifying conductance. To clarify the roles of ion channels in resonance, not only the resonant frequency but also the kinetics of conductances should be carefully examined. However, to date, few studies have focused on the kinetics of candidate conductances responsible for resonance generation.

Neurons in the inferior olive (IO) project climbing fibers to the cerebellar cortex, which forms strong excitatory synapses on Purkinje cells. IO neurons exhibit STOs ranging from 2 to 10 Hz (Benardo and Foster, 1986; Bleasel and Pettigrew, 1992; Devor and Yarom, 2002; Khosrovani et al., 2007; Llinas and Yarom, 1986). Previous analyses have demonstrated that T-type VDCCs crucial for olivo-cerebellar functions (Hildebrand et al., 2009; Ly et al.,

2013) play a pivotal role in resonance and STOs in IO neurons. They are suppressed by T-type VDCC blockers (Benardo and Foster, 1986; Choi et al., 2010; Lampl and Yarom, 1997; Llinas and Yarom, 1986; Placantonakis and Welsh, 2001), and can be theoretically reproduced in model cells with a low-threshold $Ca^{2+}$ conductance (Hutcheon et al., 1994; Manor et al., 1997). However, the STO is small, but not completely ablated in mutant mice deficient in Cav3.1 ($\alpha$1G) (Choi et al., 2010), the major alpha subunit of T-type VDCCs expressed in the IO (Talley et al., 1999). Moreover, several studies support that HCN channels are abundantly expressed (Monteggia et al., 2000; Notomi and Shigemoto, 2004; Santoro et al., 2000) and participate in rhythmic firing of IO neurons (Bal and McCormick, 1997). It remains therefore undetermined whether T-type VDCC is the major ion channel responsible for resonance in IO neurons.

In the present study, we examined ion channel behaviors potentially involved in resonance of IO neurons. Results showed that Cav3.1 T-type VDCCs strongly amplified resonance in a membrane potential-dependent manner, although their activation was less dependent on the frequency of input current or potential. These data suggest that Cav3.1 T-type VDCCs act as an amplifying conductance. The resonating conductance was mainly mediated by HCN1 channels, and the HCN1-dependent conductance exhibited properties necessary for acting as a phenomenological inductor. Additionally, Kv channels were also involved in resonating conductance, although their contribution was restrictive. These results

suggest that ion channels with distinct electrophysiological properties cooperatively contribute to resonance in IO neurons.

## Results

### Electrical resonance of IO neurons

We performed whole-cell recordings from neurons in the IO. In the current clamp mode, hyperpolarizing current injections elicited depolarizing sags as a result of hyperpolarization-activated potential (Figure S1A). Rebound low-threshold $Ca^{2+}$ spikes followed the hyperpolarizing current offset (Figure S1A) (Choi et al., 2010; Llinas and Yarom, 1981). In some cases, $Ca^{2+}$ spikes were associated with a brief damped oscillation (Figure S1A). Depolarizing current injections elicited high threshold $Ca^{2+}$ spikes (Figure S1B). The active and basic (Table S1) membrane properties of IO neurons were consistent with previous reports (Bal and McCormick, 1997; Best and Regehr, 2008; Choi et al., 2010).

To assess the electrical resonance in IO neurons, we utilized impedance amplitude profile (ZAP) stimulus (Lampl and Yarom, 1997; Puil et al., 1986) (see experimental procedures). Because voltage-dependent $Na^{+}$ channels are not involved in resonance in IO neurons (Benardo and Foster, 1986; Llinas and Yarom, 1986), TTX was always added to the extracellular solution. As previously reported (Lampl and Yarom, 1997), the impedance-frequency (*Z-F*) profile was strongly dependent on membrane potential.

Impedance was low and basically declined with input frequency at a membrane potential of –40 mV (Figures 1A–C). At –60 mV, the magnitude of the voltage response was enhanced around 3 s (roughly corresponding to 3 Hz), and the *Z-F* profile exhibited a clear hump (Figure 1C). The majority of neurons (25/27, Figure S1G) exhibited a resonant frequency > 2 Hz (Figure 1E). The resonant strength (see experimental procedures) increased with hyperpolarization of the membrane potential, which peaked at –75 mV, and then declined with further hyperpolarization (Figure 1D). The resonant frequency gradually increased with hyperpolarization (Figure 1E) (Hutcheon et al., 1996b). To examine possible developmental changes in the resonance of IO neurons, we compared *Z-F* profiles at P14–P15, P19–P20, and P30–P37. The membrane potential dependency of resonant strength and resonant frequency was not significantly different among these groups (Figure S1D), suggesting that the resonant properties were almost mature by P14–P15.

We also noticed that positive and negative voltage fluctuations were nearly symmetrical at a baseline of around –60 mV, although depolarizing deflections were clearly larger than hyperpolarizing ones around –75 mV (Figure 1A). These asymmetrical fluctuations were likely caused by regenerative potentials elicited at depolarizing phases. Interpretation of the calculated impedance in the linear RLC circuit requires an approximate linear relationship between input current and output voltage, but the generation of regenerative potentials may disturb the linear relationship (Hutcheon et al., 1996b; Strohmann

et al., 1994). Therefore, the magnitude of impedance from –65 mV to –85 mV might not be properly assessed as that in the linear RLC circuit. However, because the calculated value indicates the absolute ratio of output voltage relative to input current, this data indicates that output voltage significantly increased around a frequency of 3–5 Hz.

**Cav3.1 T-type VDCCs strongly enhance resonance**

We first examined the contribution of VDCCs to resonance in IO neurons. First, we recorded resonance in a $Ca^{2+}$-free external solution to suppress VDCC-mediated currents. The resonant strength in the $Ca^{2+}$-free solution was significantly less than in the control solution (Figures 2A, B, and E). Moreover, positive and negative voltage fluctuations were almost symmetrical at all tested membrane potentials (Figure 2A), suggesting that the regenerative potentials were mediated by $Ca^{2+}$ currents. This notion was confirmed by waveform analysis of $Ca^{2+}$-dependent components (Figures S1E and F). These waveforms essentially comprised alternate depolarizing and hyperpolarizing potentials (Figures S1E and F). Positive and negative voltage fluctuations were almost symmetrical at –60 mV, but the amplitudes of depolarizing potentials were clearly larger than hyperpolarizing potentials at –75 mV (Figures S1E and F).

We next identified the VDCC subtype responsible for resonance in IO neurons. Bath application of $Ni^{2+}$, a blocker of T-type and R-type VDCCs, strongly suppressed resonance to

a level identical to the $Ca^{2+}$-free experiment (Figure S2B). We further examined the contribution of T-type VDCCs using Cav3.1 knockout (Cav3.1 KO) mice (Petrenko et al., 2007) in which the generation of rebound $Ca^{2+}$ spikes was abolished (Figure S2A) (Choi et al., 2010). Similar to the experiment with $Ca^{2+}$-free external solution, voltage fluctuations were almost symmetrical at all tested membrane potentials in Cav3.1 KO mice (Figure 2C), indicating that the regenerative potentials were low-threshold $Ca^{2+}$ spikes (Benardo and Foster, 1986). Importantly, the membrane potential dependence of resonant strength and resonant frequency in Cav3.1 KO mice was identical to wild-type (WT) mice in the $Ca^{2+}$-free external solution (Figures 2A–F). This suggests that the Cav3.1 T-type VDCC is the major VDCC that amplifies resonance in IO neurons.

**Conductance mediated by HCN1 channels is essential for resonance**

Although resonant strength was significantly less, the *Z-F* profile still exhibited a clear hump in Cav3.1 KO mice (Figure 2D) and the resonant frequency was > 2 Hz (Figure 2F). To corroborate the linearity between input and output of remnant resonance, we applied chirp currents with amplitudes of 20, 50, and 100 pA, and compared the resulting *Z-F* profiles in Cav3.1 KO mice. Amplitudes of resulting voltage responses were linearly increased with input currents (Figure 3I), but the *Z-F* profiles were not affected by this manipulation (Figure 3J). This result ensures a linear relationship between input current and voltage responses of

residual resonance (Lampl and Yarom, 1997; Strohmann et al., 1994).

The residual resonance in Cav3.1 KO mice was not mediated by high-voltage-activated $Ca^{2+}$ channels or compensatory upregulation of other T-type VDCC subtypes, because the WT IO neurons exhibited similar resonance in the $Ca^{2+}$-free solution (Figures 2E and F). Therefore, we pharmacologically examined other possible candidates. We focused on HCN channels, because they play a crucial role in resonance in some neurons (Hu et al., 2002; Sun et al., 2012; Ulrich, 2014; Zemankovics et al., 2010). In the presence of 20 μM ZD7288, a blocker of HCN channels, the impedance declined with frequency of input currents in Cav3.1 KO mice at all tested membrane potentials (Figures 3A, C, and G). The resonant frequency was < 2 Hz (Figure 3H), indicating a disappearance of resonance. These results suggest that residual resonance in Cav3.1 KO mice is mediated by HCN channels.

To address the precedence between ZD7288-sensitive and Cav3.1-dependent responses, we administered ZD7288 to WT mice. The generation of $Ca^{2+}$ spikes was not blocked (discussed later), but the *Z-F* profile did not exhibit a clear hump in the presence of ZD7288 at all tested membrane potentials (Figures 3B and C), suggesting that HCN channel activation was essential for resonance in IO neurons (Figures 3G and H). Taken together, these results strongly suggest that the HCN channel acts as the major resonating conductance in IO neurons.

To identify the HCN channel subtype, we used mutant mice lacking HCN1, a HCN

channel subtype that is strongly expressed in the IO (Monteggia et al., 2000; Notomi and Shigemoto, 2004; Santoro et al., 2000). In the HCN1 knockout (KO) mice, there was no depolarizing sag following the hyperpolarizing current injection (Figure S2C). Responses to chirp currents (Figure 3D) were identical to WT mice with ZD7288 (Figure 3B), and there was no clear hump in the *Z-F* profile (Figure 3F). In the $Ca^{2+}$-free external solution, the generation of low threshold $Ca^{2+}$ spikes was eliminated (Figure 3E), and the *Z-F* profile (Figure 3F) was identical to Cav3.1 KO mice with ZD7288 (Figure 3C). These results strongly suggest that ZD7288-sensitive resonance is mediated by the HCN1 channel.

**Activation of T-type VDCCs is dependent on depolarization of the membrane potential**

Following administration of ZD7288 in WT mice, the frequency for $Ca^{2+}$ spike activation shifted from around 4 Hz in the control extracellular solution (Figure 1A) to a lower frequency range (Figure 3B). If the membrane does not have phenomenological inductors, namely the circuit is constructed only with resisters and capacitors, the amplitude of the voltage response is largest at the first positive peak and monotonically declines with input frequency (Hutcheon and Yarom, 2000) (Figures 3A and E). Therefore, the shift in frequency for $Ca^{2+}$ spike activation could be explained by a shift in frequency at which the membrane potential depolarization is larger (Hutcheon et al., 1996b; Ulrich, 2014). To test this possibility, we analyzed the threshold voltage of $Ca^{2+}$-dependent responses (Figures 3K–

N). In the control solution, $Ca^{2+}$ potentials were elicited at a membrane potential around -70 mV, but were not elicited at the first or second peaks that were less than the threshold potential (Figures 3K and M). In the presence of ZD7288, $Ca^{2+}$ spike activation shifted to the first peak (Figure 3L), but the thresholds remained around –70 mV (Figures 3M and N). Importantly, hyperpolarizing potentials after $Ca^{2+}$ spikes were smaller in the presence of ZD7288 (Figure 3L) or in HCN1 KO mice (Figure S2D), suggesting they were partially mediated by closure of the HCN1 channels (see discussion). These results indicated that activation of T-type VDCCs is strongly dependent on depolarization of the membrane potential, but much less on frequency of the input current.

**Voltage-clamp analysis of ZD7288-sensitive and $Ca^{2+}$-dependent currents**

To confirm the above-mentioned conclusions, ZD7288-sensitive and $Ca^{2+}$-dependent currents were directly recorded under the voltage-clamp mode. We first theoretically verified the frequency-dependence of currents that flowed through electrical equivalent circuits shown in Figure 4A. When the input voltage was clamped in a sine wave pattern (Figure 4B), current with a sinusoidal waveform mainly flowed through the inductor at a lower frequency range (Figures 4C–F and I, blue lines and symbols). The magnitude of current flowing through the inductor monotonically declined with increased frequency of input voltage (Figure 4I). Conversely, the sum of currents flowing through the capacitor and resistance monotonically

increased (Figure 4H, green symbols). As a result, the amplitude-frequency plots of total currents exhibited a bottom (Figure 4H, red symbols). In parallel, the phase of the current relative to the input voltage shifted from a lag mainly caused by the inductor to a lead as a result of the capacitor around the resonant frequency (Figure 4G, red symbols). We mainly focused on the following three current properties: i) sinusoidal waveform, ii) phase shift from lag to lead, and iii) frequency-dependence of current amplitude.

First, we examined properties of the ZD7288-sensitive current using Cav3.1 KO mice. As theoretically expected (Figure 4H, red symbols), the amplitudes of total currents in response to the sinusoidal voltage-clamp (Figure 5A) were smallest around the resonant frequency (Figures 5B–E and G). In the presence of ZD7288, amplitude of the total currents was monotonically increased (Figures 5B–E and G), which represented the response in the RC circuit (Figure 4H, green). Moreover, the phases of total currents changed from lag to lead in the control solution (Figure 5F, red), but they were always lead in the presence of ZD7288 (Figure 5F, green) (Narayanan and Johnston, 2008). The isolated ZD7288-sensitive currents exhibited nearly sinusoidal waveforms, and the peak amplitudes declined with increase in input frequency (Figures 5B–E and H, blue). These results supported the notion that the ZD7288-sensitive component exhibits properties required for a phenomenological inductor.

Next, we examined the $Ca^{2+}$-dependent current using WT mice. In contrast to the ZD7288-dependent current, the isolated $Ca^{2+}$-dependent current exhibited only inward

components (Figures 6B–E, blue) to the sinusoidal voltage-clamp (Figure 6A). $Ca^{2+}$-dependent currents were repeatedly elicited on every depolarizing phases of the clamping voltage when the depolarization overcame a threshold voltage (Figures 6F and G), suggesting strong membrane potential dependency. These results indicated that properties of $Ca^{2+}$-dependent component were not suitable for a phenomenological inductor.

**Cav3.1 and HCN1 clusters do not overlap, but are closely apposed, on dendrites of IO neurons**

To better understand the morphological basis, we examined Cav3.1 and HCN1 distributions. We first examined mRNA expression by fluorescent *in situ* hybridization, and found that virtually all IO neurons co-expressed Cav3.1 and HCN1 (Figures 7A and B). Next, we virally labeled IO neurons with GFP (Figure S3D) and visualized Cav3.1 and HCN1 distributions using specific antibodies (Figures S3A–C). HCN1 (Milligan et al., 2006) and Cav3.1 expression was revealed as a punctate appearance on dendrites (Figures 7C–E), and only occasionally overlapped (Figures 7D3 and E3). We further characterized subcellular distribution by utilizing preembedding immunogold electron microscopy. Cav3.1 (Figure S3E) and HCN1 (Figure S3F) immunoparticles were mainly associated with the plasma membrane, with higher densities on dendritic shafts and spines than on the soma (Figures S3G and H). We then performed SDS-digested freeze-replica immunogold-labeling

(SDS-FRL) to quantify two-dimensional distribution of Cav3.1 and HCN1 on the plasma membrane of dendrites. Cav3.1- or HCN1 immunogold particles frequently formed distinct clusters on the P-face of dendrites in WT mice (Figure 7F), and these clusters were not observed in corresponding KO mice (Figures S3I and J). Measurements of nearest neighbor distances between clusters revealed that most were located within 0.6 μm of each other (Figures 7G and H). These results morphologically confirmed a close functional relationship between channels on IO dendrites.

**Contribution of voltage-dependent potassium channels to resonance**

We then examined the contributions of other factors potentially involved in STOs or resonance. Previous studies show that electrical coupling through gap junctions significantly influence STOs in IO neurons (Bazzigaluppi et al., 2012; De Zeeuw et al., 2003; Leznik and Llinas, 2005; Long et al., 2002; Placantonakis et al., 2006). Our results, however, showed that carbenoxolone (100 μM), a gap junction blocker, did not affect resonance in IO neurons (Figure S4). Next, we examined the possible contributions of $K^+$ channels (Hu et al., 2002; Puil et al., 1988). Bath-applied UCL1684, a blocker of SK-type $Ca^{2+}$-activated $K^+$ channels, or intracellular loading of BAPTA did not block resonance in WT mice (Figure S5), suggesting that $Ca^{2+}$-activated $K^+$ channel activation plays a negligible role, if any, in resonance. Conversely, intracellular loading of tetraethylammonium (TEA), a broad-spectrum

blocker of Kv channels (Hille, 2001), suppressed remnant resonance in Cav3.1 KO mice (Figures S6C and D). Kv channels strongly expressed in the IO include Kcnd2 (Kv4.2), Kcnd3 (Kv4.3), Kcnq3, and Kcnh7 (Kv11.3) (Allen Mouse Brain Atlas (available from: http://mouse.brain-map.org.)(Lein et al., 2007)). However, the Kv4 blocker heteropodatoxin and the Kv7 blocker linopiridine did not alter the resonance (Figure S6E), but the Kv11 blocker E-4031 had an effect similar to TEA (Figures S6A–E). Although ZD7288 blocked resonance in all tested membrane potentials, TEA and E-4031 were less effective at hyperpolarized potentials (Figures S6A–D). Finally, we examined the components affected by these blockers. In the voltage-clamp mode, ZD7288 or E-4031 suppressed both inward and outward currents (Figure S6F). Suppression by E-4031 and ZD7288 were occluded (Figure S6G), suggesting that tight functional coupling between HCN and Kv channels plays a role in controlling resonance. Taken together, these results suggest that Kv channels modulate resonance around the resting membrane potential.

## Discussion

### Cav3.1 acts as an amplifying conductance

In the present study, resonance in IO neurons was greatly suppressed, but not completely abolished, in WT IO neurons in $Ca^{2+}$-free external solution (Figures 2E and F). This manipulation did not shift the resonant frequency (Figure 2F), but ZD7288 completely

blocked resonance (Figures 3G and H), which suggests that T-type VDCCs strongly enhance resonance, but do not act as a resonating conductance. The $Ca^{2+}$-dependent currents were almost inward and were only activated when the membrane potential exceeded the threshold (Figures 3K–N and 6F–G). The frequency dependence of the $Ca^{2+}$-dependent component is not very strong, because ZD7288 shifts the generation of $Ca^{2+}$ spikes to a lower frequency range. These properties are not suitable for resonating conductance, but rather enable Cav3.1 T-type VDCCs to act as an amplifying conductance. Cav3.1 might strongly enhance the small depolarizations induced by HCN1-dependent basal resonance.

Conversely, Cav3.1 might also influence HCN1 activation. Results showed that each Cav3.1-mediated $Ca^{2+}$ spike was followed by a hyperpolarizing potential (Figures S1E and F). Because the hyperpolarizing potential was suppressed by ZD7288 (Figure 3L) and the amplitude was small in HCN1 KO mice (Figure S2D), it is likely to be mediated mainly by HCN1 channels. The duration of depolarizing (119 ± 20 ms (n = 5, mean ± SEM)) and hyperpolarizing (157 ± 20 ms) potentials of the $Ca^{2+}$ spike were identical ($p$ = 0.14, Mann–Whitney U-test), and the total duration was 280 ms, which approximately corresponds to 4 Hz. Therefore, around the resonant frequency, the $Ca^{2+}$ spike is in phase with the voltage oscillation and can most effectively amplify the voltage responses. Importantly, previous reports suggested that HCN channels are partially activated at the resting potential, and strong depolarization facilitates their closure (Bal and McCormick, 1997). Partial activation of

HCN1 at the resting membrane potential is also supported by the hyperpolarized membrane potential of HCN1 KO mice (Table S1). Large depolarization by Cav3.1 activation might facilitate HCN1 closure.

Our morphological analysis demonstrates that Cav3.1 and HCN1 are located on dendritic compartments and are close enough to electrically interact (Figure 7). This distribution might be a basis for tight functional coupling between Cav3.1 and HCN1. In some models of the IO neuron, T-type VDCCs are located on somatic compartments (De Gruijl et al., 2012; Schweighofer et al., 1999). However, the present study reveals that Cav3.1 is distributed on dendrites. Thus, the model of the IO neuron should be revised, taking into account the precise subcellular localization of Cav3.1 and HCN1.

**HCN1 is a major component for frequency-dependent resonating conductance**

Although resonance in the Cav3.1 KO mice was significantly less than in WT mice, it was clearly present and completely blocked by ZD7288 (Figures 3G and H). This indicates that the remnant resonance is attributable to HCN channels, and their activation can induce resonance without Cav3.1. Moreover, resonance in WT mice was blocked by ZD7288 (Figure 3B, C) and impaired in HCN1 KO mice (Figures 3D and F), suggesting that HCN1 is essential for resonance. The *Z-F* profiles of HCN1-dependent resonance were constant when the input current amplitudes were changed (Figures 3I and J), which is consistent with a linear

relationship between input current and output voltage. Moreover, it also suggests that HCN channel activation is strongly dependent on frequency rather than on magnitude (at least within ± 10 mV) of membrane potential. Our voltage-clamp analysis revealed that the ZD7288-sensitive current exhibited frequency properties identical to that flowing in the inductor in the parallel resonant circuit (Figure 5). These lines of evidence indicate that HCN1 conductance exhibits properties enough to act as a resonating conductance. Previous reports suggest that the HCN channel acts as a resonating conductance in several neuronal types (Marcelin et al., 2012; Nolan et al., 2007; Ulrich, 2002; Zemankovics et al., 2010). Moreover, theoretical analyses demonstrate that the HCN channel can reproduce resonance (Hutcheon et al., 1996a; Narayanan and Johnston, 2008). The HCN channel may be widely shared as a common resonating conductance in many brain regions. However, a previous study concluded that HCN channels do not play a major role in resonance in IO neurons (Lampl and Yarom, 1997). This discrepancy might be due to differences in animal species and/or channel blockers used in the experiments.

The present analysis demonstrates that Kv channels influence resonating conductance, with the most likely candidate being Kv11 (Kcnh) (Figure S6). However, although ZD7288 completely blocked resonance at all of tested membrane potentials, TEA or E-4031 blocking was weaker with hyperpolarization of the membrane potentials (Figure S6C, D), suggesting that Kv channel contribution is restrictive. The question remains as to how

HCN and Kv channels are involved in resonance around a resting potential. Because ZD7288 or E-4031 alter inward and outward currents (Figure S6F), and the blocking effect of E-4031 was not additive to ZD7288 (Figure S6G), the functional interplay between HCN and Kv channels should be so tight that blockade of either channel alone could disrupt resonance in IO neurons. Membrane potential-dependent alteration of ion channels mediating resonance has been reported in several neuronal types (Hu et al., 2002; Xue et al., 2012). Because the resting membrane potential of IO neurons is near the activation limit of HCN channels, support by Kv channels might be required to ensure sufficient opening of the HCN channels.

**Ionic mechanisms underlying subthreshold oscillations**

Hutcheon and Yarom proposed that a stable STO requires interplay between resonating and amplifying conductances (Hutcheon and Yarom, 2000). Therefore, HCN1 and Cav3.1 channels might also participate in the generation of STOs in IO neurons. In IO neurons, STOs are dependent on VDCCs (Benardo and Foster, 1986; Choi et al., 2010; Lampl and Yarom, 1997; Llinas and Yarom, 1986; Placantonakis and Welsh, 2001) and rhythmic firing is affected by HCN channels (Bal and McCormick, 1997). In addition, STOs also show a similar waveform transition to that observed in resonance when membrane potential is hyperpolarized. STO waveforms are nearly sinusoidal at resting potentials, but depolarizing phases become larger at more hyperpolarized membrane potentials (Benardo and Foster,

1986; Bleasel and Pettigrew, 1992; Lampl and Yarom, 1997). These lines of evidence suggest that resonance and STO in IO neurons share common ionic mechanisms.

However, there are also several differences between resonance and STO. Previous studies show that IO neurons generate STOs with a wide frequency range from 2 to 10 Hz (Devor and Yarom, 2002; Placantonakis et al., 2000). However, resonant frequency has a narrower normal distribution that peaks around 3 Hz (Figure S1G), which does not cover the higher frequency range (8–10 Hz). Moreover, some IO neurons exhibit multi-peaks in the power spectra (Bleasel and Pettigrew, 1992; Lampl and Yarom, 1997), but the *Z-F* profile has a single peak, suggesting that neuronal membranes do not have the intrinsic resonant property to respond to two or more frequencies at once. These results suggest that STO frequency is more variable than what was theoretically predicted from resonant frequency, and that factors other than resonance might contribute to STOs in neurons. Electrical coupling through gap junctions appears to be an additional factor that enables neurons to generate STOs with a wide frequency range. Although we showed that resonance in IO neurons was not dependent on gap junctions (Figure S4), previous reports suggest that gap junction modulation alters membrane potential dependency of STO frequency (De Zeeuw et al., 2003; Leznik and Llinas, 2005; Long et al., 2002; Placantonakis et al., 2006) and the bursting pattern of IO neurons (Bazzigaluppi et al., 2012). Further studies are required to identify additional factors and to elucidate the mechanisms of STOs.

## Experimental procedures

Detailed methods are described in the Supplemental Experimental Procedures.

## Animals

All animal experiments were performed in accordance with guidelines from the experimental animal ethics committees of Hiroshima University, Hokkaido University, Fukushima Medical University, The University of Tokyo, and Niigata University. C57BL/6 mice were used in most experiments. Details for the generation of Cav3.1 KO mice (RBRC01465, Riken BRC) (Petrenko et al., 2007) and HCN1 KO mice (#016566, Jackson Laboratory) (Nolan et al., 2003) have been previously described.

## Electrophysiology

Coronal brain slices including the IO were prepared from C57BL/6, Cav3.1 KO, and HCN1 KO mice at P14–P37. The mice were anaesthetized with $CO_2$ gas and subsequently decapitated. A tissue block that included the medulla was sliced in the sucrose-based cutting solution. Whole-cell recordings were made from neurons in the principal and the dorsal accessory nuclei of the IO using an upright microscope equipped with an IR-CCD camera system. The properties of resonance were not significantly different between the IO subnuclei (Figure S1C). NBQX (10 μM), (R)-CPP (5 μM), bicuculline methchloride (10 μM) and

Tetrodotoxin (TTX, 0.5 μM) were added to the external solution for analyzing resonance.

**Impedance measurement**

Impedance was measured when neurons did not show the STO as previously described (Hutcheon and Yarom, 2000; Lampl and Yarom, 1997; Puil et al., 1986). A sinusoidal current with a constant amplitude (50 pA), but linearly altered frequency at a range of 0 to 40 Hz in 40 s (a chirp current), was applied in the current-clamp mode. Impedance ($\dot{Z}(f)$) was calculated by dividing the Fast Fourier Transform (FFT) of the voltage response by the FFT of the chirp current. Magnitude of impedance was calculated as follows:

$$\left|\dot{Z}(f)\right| = \sqrt{(Re(\dot{Z}(f))^2 + (Im(\dot{Z}(f))^2} \ ,$$

where $Re(\dot{Z}(f))$ and $Im(\dot{Z}(f))$ are real and imaginary parts of impedance, respectively. $f$ represents frequency of input current. The frequency (> 1 Hz) at which impedance reached a maximum was termed the 'resonant frequency.' Resonant strength was calculated as the ratio of maximum impedance amplitude at a resonant frequency relative to the impedance amplitude at 1 Hz.

**Antibodies**

We used the following primary antibodies: guinea pig anti-Cav3.1 (Hildebrand et al., 2009), goat anti-GFP (Takasaki et al., 2010), rabbit anti-HCN1 against amino acid residues 888–910 of mouse HCN1 (NP_034538), and commercial rabbit anti-HCN1 (APC-056, Alomone).

**Fluorescent *in situ* hybridization**

Under deep diethyl ether anesthesia, the brains were immediately frozen in powdered dry ice. Frozen sections were cut on a cryostat. Non-isotopic *in situ* hybridization was employed with fluorescein- and digoxigenin (DIG)-labeled cRNA probes for Cav3.1 and HCN1 mRNAs.

**Immunofluorescence**

Under deep pentobarbital anesthesia, mice were fixed and coronal sections were prepared. Sections were incubated overnight with a mixture of primary antibodies, followed by incubation with fluorescent secondary antibodies for 2 hr. Images were taken with a laser-scanning microscope.

**Preembedding immunogold electron microscopy**

Under deep pentobarbital anesthesia, mice were fixed and coronal sections were

prepared. Sections were incubated overnight with primary antibodies, followed by secondary antibodies linked to 1.4-nm gold particles for 4 h. Immunogolds were intensified with a silver enhancement kit. Sections were treated with osmium tetroxide, stained with uranyl acetate, and finally embedded in Epon 812. Photographs were taken with an electron microscope.

**SDS-digested freeze-fracture replica labeling**

Under deep pentobarbital anesthesia, mice were fixed and coronal sections were prepared. Sections were immersed in graded glycerol, and then rapidly frozen. Frozen samples were fractured into two parts at –140°C and replicated by carbon deposition, platinum, and carbon. Tissue debris was dissolved, and the replicas were washed in graded polyethylene glycol in washing buffer. The replicas were then incubated with anti-HCN1 antibody, followed by incubation with gold particle-conjugated secondary antibody. Cav3.1 was similarly immunolabeled using anti-Cav3.1 antibody. Photographs were taken with an electron microscope.

**Statistical analysis**

Averaged data are presented as mean ± SEM. Statistical significance was assessed using the Mann–Whitney U-test. Differences between groups were assessed by one-way ANOVA and judged to be significant at $p < 0.05$. When the difference was judged significant,

data was processed using the Holm-Sidak test as a post-hoc test. One and two asterisks represent $p < 0.05$ and $p < 0.01$, respectively. In morphological analysis, differences between groups were assessed using the Steel-Dwass test.

## Author Contributions

Y.M-M. and K.H. designed the study. Y.M-M., M.Y., and T.M. performed the research. K.K., M.W., M.K., and K.S. contributed reagents/analytical tools. Y.M-M., H.N., M.Y., T.M., K.K., M.W., M.K., K.S., and K.H. wrote the manuscript.

## Acknowledgements

We thank R. Kubo, K. Yamaoka, Y. Yoshioka, Y. Matsumoto, and T. Hirakawa for technical assistance, as well as Y. Fukazawa and R. Shigemoto for technical advice. This work was supported by Grants-in-Aid for Scientific Research (25000015 to M.K. and K.H., 25117006 to K.H., 15K18342 to H.N.) and the Strategic Research Program for Brain Sciences from MEXT and AMED, Japan.

**References**

Bal, T., and McCormick, D.A. (1997). Synchronized oscillations in the inferior olive are controlled by the hyperpolarization-activated cation current I(h). J. Neurophysiol. *77*, 3145-3156.

Bazzigaluppi, P., De Gruijl, J.R., van der Giessen, R.S., Khosrovani, S., De Zeeuw, C.I., and de Jeu, M.T. (2012). Olivary subthreshold oscillations and burst activity revisited. Front Neural Circuits *6*, 91.

Benardo, L.S., and Foster, R.E. (1986). Oscillatory behavior in inferior olive neurons: mechanism, modulation, cell aggregates. Brain Res. Bull. *17*, 773-784.

Best, A.R., and Regehr, W.G. (2008). Serotonin evokes endocannabinoid release and retrogradely suppresses excitatory synapses. J. Neurosci. *28*, 6508-6515.

Bleasel, A.F., and Pettigrew, A.G. (1992). Development and properties of spontaneous oscillations of the membrane potential in inferior olivary neurons in the rat. Brain Res. Dev. Brain Res. *65*, 43-50.

Buzsaki, G. (2006). Rhythms of the brain (New York: Oxford University Press).

Choi, S., Yu, E., Kim, D., Urbano, F.J., Makarenko, V., Shin, H.S., and Llinas, R.R. (2010). Subthreshold membrane potential oscillations in inferior olive neurons are dynamically regulated by P/Q- and T-type calcium channels: a study in mutant mice. J. Physiol. *588*, 3031-3043.

De Gruijl, J.R., Bazzigaluppi, P., de Jeu, M.T., and De Zeeuw, C.I. (2012). Climbing fiber burst size and olivary sub-threshold oscillations in a network setting. PLoS Comput. Biol. *8*, e1002814.

De Zeeuw, C.I., Chorev, E., Devor, A., Manor, Y., Van Der Giessen, R.S., De Jeu, M.T., Hoogenraad, C.C., Bijman, J., Ruigrok, T.J., French, P.*, et al.* (2003). Deformation of network connectivity in the inferior olive of connexin 36-deficient mice is compensated by morphological and electrophysiological changes at the single neuron level. J. Neurosci. *23*, 4700-4711.

Devor, A., and Yarom, Y. (2002). Generation and propagation of subthreshold waves in a network of inferior olivary neurons. J. Neurophysiol. *87*, 3059-3069.

Erchova, I., Kreck, G., Heinemann, U., and Herz, A.V. (2004). Dynamics of rat entorhinal cortex layer II and III cells: characteristics of membrane potential resonance at rest predict oscillation properties near threshold. J. Physiol. *560*, 89-110.

Gutfreund, Y., yarom, Y., and Segev, I. (1995). Subthreshold oscillations and resonant frequency in guinea-pig cortical neurons: physiology and modelling. J. Physiol. *483 ( Pt 3)*, 621-640.

Hildebrand, M.E., Isope, P., Miyazaki, T., Nakaya, T., Garcia, E., Feltz, A., Schneider, T., Hescheler, J., Kano, M., Sakimura, K.*, et al.* (2009). Functional coupling between mGluR1 and Cav3.1 T-type calcium channels contributes to parallel fiber-induced fast calcium

signaling within Purkinje cell dendritic spines. J. Neurosci. *29*, 9668-9682.

Hille, B. (2001). Ion Channels of Exitable membranes, 3rd ed. (Sinauer Associates, Inc.).

Hu, H., Vervaeke, K., and Storm, J.F. (2002). Two forms of electrical resonance at theta frequencies, generated by M-current, h-current and persistent $Na^+$ current in rat hippocampal pyramidal cells. J. Physiol. *545*, 783-805.

Hutcheon, B., Miura, R.M., and Puil, E. (1996a). Models of subthreshold membrane resonance in neocortical neurons. J. Neurophysiol. *76*, 698-714.

Hutcheon, B., Miura, R.M., and Puil, E. (1996b). Subthreshold membrane resonance in neocortical neurons. J. Neurophysiol. *76*, 683-697.

Hutcheon, B., Miura, R.M., Yarom, Y., and Puil, E. (1994). Low-threshold calcium current and resonance in thalamic neurons: a model of frequency preference. J. Neurophysiol. *71*, 583-594.

Hutcheon, B., and Yarom, Y. (2000). Resonance, oscillation and the intrinsic frequency preferences of neurons. Trends Neurosci. *23*, 216-222.

Khosrovani, S., Van Der Giessen, R.S., De Zeeuw, C.I., and De Jeu, M.T. (2007). In vivo mouse inferior olive neurons exhibit heterogeneous subthreshold oscillations and spiking patterns. Proc. Natl. Acad. Sci. U. S. A. *104*, 15911-15916.

Lampl, I., and Yarom, Y. (1997). Subthreshold oscillations and resonant behavior: two manifestations of the same mechanism. Neuroscience *78*, 325-341.

Lein, E.S., Hawrylycz, M.J., Ao, N., Ayres, M., Bensinger, A., Bernard, A., Boe, A.F., Boguski, M.S., Brockway, K.S., Byrnes, E.J., *et al.* (2007). Genome-wide atlas of gene expression in the adult mouse brain. Nature *445*, 168-176.

Leznik, E., and Llinas, R. (2005). Role of gap junctions in synchronized neuronal oscillations in the inferior olive. J. Neurophysiol. *94*, 2447-2456.

Llinas, R., and Yarom, Y. (1981). Properties and distribution of ionic conductances generating electroresponsiveness of mammalian inferior olivary neurones in vitro. J. Physiol. *315*, 569-584.

Llinas, R., and Yarom, Y. (1986). Oscillatory properties of guinea-pig inferior olivary neurones and their pharmacological modulation: an in vitro study. J. Physiol. *376*, 163-182.

Llinas, R.R. (1988). The intrinsic electrophysiological properties of mammalian neurons: insights into central nervous system function. Science *242*, 1654-1664.

Long, M.A., Deans, M.R., Paul, D.L., and Connors, B.W. (2002). Rhythmicity without synchrony in the electrically uncoupled inferior olive. J. Neurosci. *22*, 10898-10905.

Ly, R., Bouvier, G., Schonewille, M., Arabo, A., Rondi-Reig, L., Lena, C., Casado, M., De Zeeuw, C.I., and Feltz, A. (2013). T-type channel blockade impairs long-term potentiation at the parallel fiber-Purkinje cell synapse and cerebellar learning. Proc. Natl. Acad. Sci. U. S. A. *110*, 20302-20307.

Manor, Y., Rinzel, J., Segev, I., and Yarom, Y. (1997). Low-amplitude oscillations in the

inferior olive: a model based on electrical coupling of neurons with heterogeneous channel densities. J. Neurophysiol. *77*, 2736-2752.

Marcelin, B., Liu, Z., Chen, Y., Lewis, A.S., Becker, A., McClelland, S., Chetkovich, D.M., Migliore, M., Baram, T.Z., Esclapez, M., and Bernard, C. (2012). Dorsoventral differences in intrinsic properties in developing CA1 pyramidal cells. J. Neurosci. *32*, 3736-3747.

Milligan, C.J., Edwards, I.J., and Deuchars, J. (2006). HCN1 ion channel immunoreactivity in spinal cord and medulla oblongata. Brain Res. *1081*, 79-91.

Monteggia, L.M., Eisch, A.J., Tang, M.D., Kaczmarek, L.K., and Nestler, E.J. (2000). Cloning and localization of the hyperpolarization-activated cyclic nucleotide-gated channel family in rat brain. Brain Res. Mol. Brain Res. *81*, 129-139.

Narayanan, R., and Johnston, D. (2008). The h channel mediates location dependence and plasticity of intrinsic phase response in rat hippocampal neurons. J. Neurosci. *28*, 5846-5860.

Nolan, M.F., Dudman, J.T., Dodson, P.D., and Santoro, B. (2007). HCN1 channels control resting and active integrative properties of stellate cells from layer II of the entorhinal cortex. J. Neurosci. *27*, 12440-12451.

Nolan, M.F., Malleret, G., Lee, K.H., Gibbs, E., Dudman, J.T., Santoro, B., Yin, D., Thompson, R.F., Siegelbaum, S.A., Kandel, E.R., and Morozov, A. (2003). The hyperpolarization-activated HCN1 channel is important for motor learning and neuronal integration by cerebellar Purkinje cells. Cell *115*, 551-564.

Notomi, T., and Shigemoto, R. (2004). Immunohistochemical localization of Ih channel subunits, HCN1-4, in the rat brain. J. Comp. Neurol. *471*, 241-276.

Petrenko, A.B., Tsujita, M., Kohno, T., Sakimura, K., and Baba, H. (2007). Mutation of α1G T-type calcium channels in mice does not change anesthetic requirements for loss of the righting reflex and minimum alveolar concentration but delays the onset of anesthetic induction. Anesthesiology *106*, 1177-1185.

Placantonakis, D., and Welsh, J. (2001). Two distinct oscillatory states determined by the NMDA receptor in rat inferior olive. J. Physiol. *534*, 123-140.

Placantonakis, D.G., Bukovsky, A.A., Aicher, S.A., Kiem, H.P., and Welsh, J.P. (2006). Continuous electrical oscillations emerge from a coupled network: a study of the inferior olive using lentiviral knockdown of connexin36. J. Neurosci. *26*, 5008-5016.

Placantonakis, D.G., Schwarz, C., and Welsh, J.P. (2000). Serotonin suppresses subthreshold and suprathreshold oscillatory activity of rat inferior olivary neurones in vitro. J. Physiol. *524 Pt 3*, 833-851.

Puil, E., Gimbarzevsky, B., and Miura, R.M. (1986). Quantification of membrane properties of trigeminal root ganglion neurons in guinea pigs. J. Neurophysiol. *55*, 995-1016.

Puil, E., Gimbarzevsky, B., and Spigelman, I. (1988). Primary involvement of $K^+$ conductance in membrane resonance of trigeminal root ganglion neurons. J. Neurophysiol. *59*, 77-89.

Santoro, B., Chen, S., Luthi, A., Pavlidis, P., Shumyatsky, G.P., Tibbs, G.R., and Siegelbaum,

S.A. (2000). Molecular and functional heterogeneity of hyperpolarization-activated pacemaker channels in the mouse CNS. J. Neurosci. *20*, 5264-5275.

Schweighofer, N., Doya, K., and Kawato, M. (1999). Electrophysiological properties of inferior olive neurons: A compartmental model. J. Neurophysiol. *82*, 804-817.

Strohmann, B., Schwarz, D.W., and Puil, E. (1994). Subthreshold frequency selectivity in avian auditory thalamus. J. Neurophysiol. *71*, 1361-1372.

Sun, H., Luhmann, H.J., and Kilb, W. (2012). Resonance properties of different neuronal populations in the immature mouse neocortex. Eur. J. Neurosci. *36*, 2753-2762.

Takasaki, C., Yamasaki, M., Uchigashima, M., Konno, K., Yanagawa, Y., and Watanabe, M. (2010). Cytochemical and cytological properties of perineuronal oligodendrocytes in the mouse cortex. Eur. J. Neurosci. *32*, 1326-1336.

Talley, E.M., Cribbs, L.L., Lee, J.H., Daud, A., Perez-Reyes, E., and Bayliss, D.A. (1999). Differential distribution of three members of a gene family encoding low voltage-activated (T-type) calcium channels. J. Neurosci. *19*, 1895-1911.

Ulrich, D. (2002). Dendritic resonance in rat neocortical pyramidal cells. J. Neurophysiol. *87*, 2753-2759.

Ulrich, D. (2014). Subthreshold delta-frequency resonance in thalamic reticular neurons. Eur. J. Neurosci. *40*, 2600-2607.

Wang, X.J. (2010). Neurophysiological and computational principles of cortical rhythms in

cognition. Physiol. Rev. *90*, 1195-1268.

Xue, W.N., Wang, Y., He, S.M., Wang, X.L., Zhu, J.L., and Gao, G.D. (2012). SK- and h-current contribute to the generation of theta-like resonance of rat substantia nigra pars compacta dopaminergic neurons at hyperpolarized membrane potentials. Brain Struct Funct *217*, 379-394.

Zemankovics, R., Kali, S., Paulsen, O., Freund, T.F., and Hajos, N. (2010). Differences in subthreshold resonance of hippocampal pyramidal cells and interneurons: the role of h-current and passive membrane characteristics. J. Physiol. *588*, 2109-2132.

**Figure legends**

**Figure 1**. **Resonance in IO neurons.**

(**A**) Representative voltage waves in response to chirp current (50 pA) at membrane potentials of –40, –60, –75, and –90 mV. (**B**) *Z-F* profiles calculated from traces in A. (**C**) Average *Z-F* profiles (n = 27 cells). Shaded area indicates mean ± SEM. (**D, E**) Membrane potential dependency of resonant strength (D) and resonant frequency (E). Number of cells is 17 at –50, –65, –70, –80, and –85 mV, and 27 at –40, –60, –75, and –90 mV. Averaged data are presented as mean ± SEM. See also Figure S1, S4, S5, and Table S1.

**Figure 2. Cav3.1 acts as an amplifying conductance.**

(**A**) Representative voltage traces of a WT IO neuron in the $Ca^{2+}$-free external solution at membrane potentials of –40, –60, –75, and –90 mV. (**B**) Average *Z-F* profiles (n = 11 cells). Dotted lines represent aforementioned WT data in control solution (Figure 1C). Shaded area indicates mean ± SEM. (**C**) Similar to A, but voltage traces recorded from an IO neuron in a Cav3.1 KO mouse. (**D**) Averaged *Z-F* profiles of Cav3.1 KO mice (n = 19). (**E, F**) Membrane potential dependency of resonant strength (E) and resonant frequency (F) in WT mice in $Ca^{2+}$-free external solution (n = 11) and Cav3.1 KO mice (n = 19). Data for WT mice (dotted line) in E and F are the same as in Figures 1D and 1E, respectively. Averaged data are presented as mean ± SEM. See also Figure S2, S4, and S5.

**Figure 3. Contribution of HCN1 in resonance.**

(**A**) Representative voltage traces in response to chirp currents in the presence of ZD7288 (20 μM) in a Cav3.1 KO IO neuron. (**B**) Similar to A, but voltage response of a WT IO neuron in the presence of ZD7288. (**C**) Average *Z-F* profiles of WT (black, n = 5) and Cav3.1 KO (green, n = 11) IO neurons in ZD7288. Shaded area indicates mean ± SEM. (**D**) Voltage responses of an HCN1 KO neuron. (**E**) Voltage responses of an HCN1 KO neuron in the $Ca^{2+}$-free solution. (**F**) Average *Z-F* profiles of HCN1 KO neurons in normal (reddish brown, n = 9) and $Ca^{2+}$-free (orange, n = 7) external solutions. (**G, H**) Membrane potential dependency of resonant strength (G) and resonant frequency (H). Data for WT and Cav3.1 KO mice (dotted lines) in G and H are the same in Figures 1D and 2E, and 1E and 2F, respectively. (**I**) Average traces in response to chirp currents with amplitudes of 25 (upper), 50 (middle), and 100 pA (lower) at –75 mV (n = 5). (**J**) Average *Z-F* profiles for input currents of 25 (black), 50 (red), and 100 (blue) pA (n = 5). (**K**) Representative voltage traces recorded in normal (red) and $Ca^{2+}$-free (gray) external solutions at –75 mV in a WT IO neuron (upper). Second derivative of $Ca^{2+}$-dependent component (lower). Threshold voltages are estimated from the second derivative of the $Ca^{2+}$-dependent components. (**L**) Similar to K, but data recorded in the presence of ZD7288. (**M**) Threshold potentials for $Ca^{2+}$-dependent components in normal solution (red) and in the presence of ZD7288 (blue) are plotted against

the observed times. Membrane potentials recorded from each IO neuron are connected. (**N**) No significant difference in average threshold potentials in normal solution (n = 5) and in the presence of ZD7288 (n = 5, $p$ = 0.41 Mann–Whitney U-test). Open and closed symbols represent data from individual cells and averaged values, respectively. Averaged data are presented as mean ± SEM. See also Figure S2 and S6.

**Figure 4. Simulation of currents in the RLC circuit under voltage clamp.**

(**A**) RLC circuit with a leaky inductor ($R_L$ and $L$) and resistance of the recording electrode ($R_e$) (left). RC circuit representing a membrane whose inductive element is blocked (right). (**B**) Waveform of input voltage. (**C–F**) (upper) Calculated total currents ($I_{total}$) flowing in the RLC (red) and RC (green) circuits. Frequencies of input voltages are 1 Hz (C), 7 Hz (D), 15 Hz (E), and 20 Hz (F), respectively. Calculated currents flowing in the inductor ($I_L$) (lower). (**G, H**) Phase (G) and amplitude (H) profiles of the $I_{total}$ flowing in the RLC (red) and RC (green) circuits to the input voltage frequency. Sum of $I_R$ and $I_C$ in the RLC circuit (purple) is almost identical to $I_{total}$ in the RC circuit. (**I**) Frequency dependence of amplitudes of current flowing in the leaky inductor in the RLC circuit ($I_L$).

**Figure 5. Voltage clamp recordings of the ZD7288-sensitive current.**

(**A**) Sinusoidal waveform of the holding potential at −75 mV. (**B–E**) Representative currents in

response to the sinusoidal voltage clamp (± 15 mV) with a frequency of 1 Hz (B), 5 Hz (C), 10 Hz (D), and 15 Hz (E) in a Cav3.1 KO IO neuron. To avoid transient responses, waves from the $4^{th}$ to the $8^{th}$ cycles of the input voltage were analyzed. Currents in control (red) and ZD7288-containing (green) solutions (upper). ZD7288-sensitive currents (blue) are calculated by subtracting current recorded in the presence of ZD7288 from the control solution (lower). (**F**) Phase of membrane current relative to frequency of holding potential in control (red) and ZD7288-containing (green) solutions (n = 8). The phase is estimated from cross-correlation analysis. (**G**) Amplitude of membrane current is plotted against frequency of holding potential. The half-magnitude from the bottom to the top of the sinusoidal membrane current represents amplitude. (**H**) Frequency-dependence of amplitudes of ZD7288-sensitive currents. Averaged data are presented as mean ± SEM. $^{**}p < 0.01$. See also Figure S6.

**Figure 6. Voltage clamp recordings of $Ca^{2+}$-dependent current.**

(**A**) Sinusoidal waveform of the holding potential at –75 mV. (**B–E**) Representative currents in response to the sinusoidal voltage clamp with 1 Hz (B), 5 Hz (C), 10 Hz (D), and 15 Hz (E) in a WT IO neuron. Membrane currents recorded in control (red) and $Ca^{2+}$-free external (green) solutions (upper). $Ca^{2+}$-dependent currents are calculated by subtracting the wave recorded in $Ca^{2+}$-free external solution from the normal external solution (lower). (**F**) Representative $Ca^{2+}$-dependent current (blue) (upper). Second derivative of the $Ca^{2+}$-dependent current

(middle). Holding potential (lower). Threshold voltages are estimated by the 2nd derivative of the $Ca^{2+}$-dependent currents. (**G**) Thresholds of $Ca^{2+}$-dependent currents are plotted against cycles of the holding potential (n = 5). Black and red symbols represent data from individual cells and averaged values, respectively. $Ca^{2+}$-dependent components are repeatedly elicited at the same threshold ($p$ = 0.998 (1 Hz), $p$ = 0.983 (5 Hz), $p$ = 0.928 (10 Hz), $p$ = 0.283 (15 Hz), one-way ANOVA) and a latency relative to the cycle ($p$ = 0.998 (1 Hz), $p$ = 0.983 (5 Hz), $p$ = 0.925 (10 Hz), $p$ = 0.296 (15 Hz), one-way ANOVA). Averaged data are presented as mean ± SEM.

**Figure 7. Cav3.1 and HCN1 distribution in the IO.**

(**A, B**) Double-labeling FISH for Cav3.1 ($A_1$) and HCN1 ($A_2$) mRNA expression in the IO. At a higher magnification, Cav3.1 (red) and HCN1 (green) mRNA are co-expressed in IO neurons (B). (**C–E**) Triple immunofluorescence showing Cav3.1 and HCN1 localization on dendrites of GFP-labeled neurons. Squared areas in C are shown in D and E. Arrows and arrowheads indicate Cav3.1- and HCN1-positive puncta, respectively. (**F**) SDS-FRL confirms Cav3.1 and HCN1 localization on the dendritic plasma membrane. Immunogold clusters for Cav3.1 and HCN1 are pseudocolored in green and red, respectively. (**G, H**) Summary histograms show the nearest-neighbor distance measured from Cav3.1- to HCN1-positive clusters (F) and *vice versa* (G) on IO dendrites. A total of 58 Cav3.1-positive and 87

HCN1-positive clusters containing two or more immunogold particles were analyzed from 10 dendrites (average of 2 μm) in two mice. Scale bars, A, 100 μm; B, 20 μm; C, 10 μm; D and E, 2 μm; F, 500 nm. See also Figure S3.

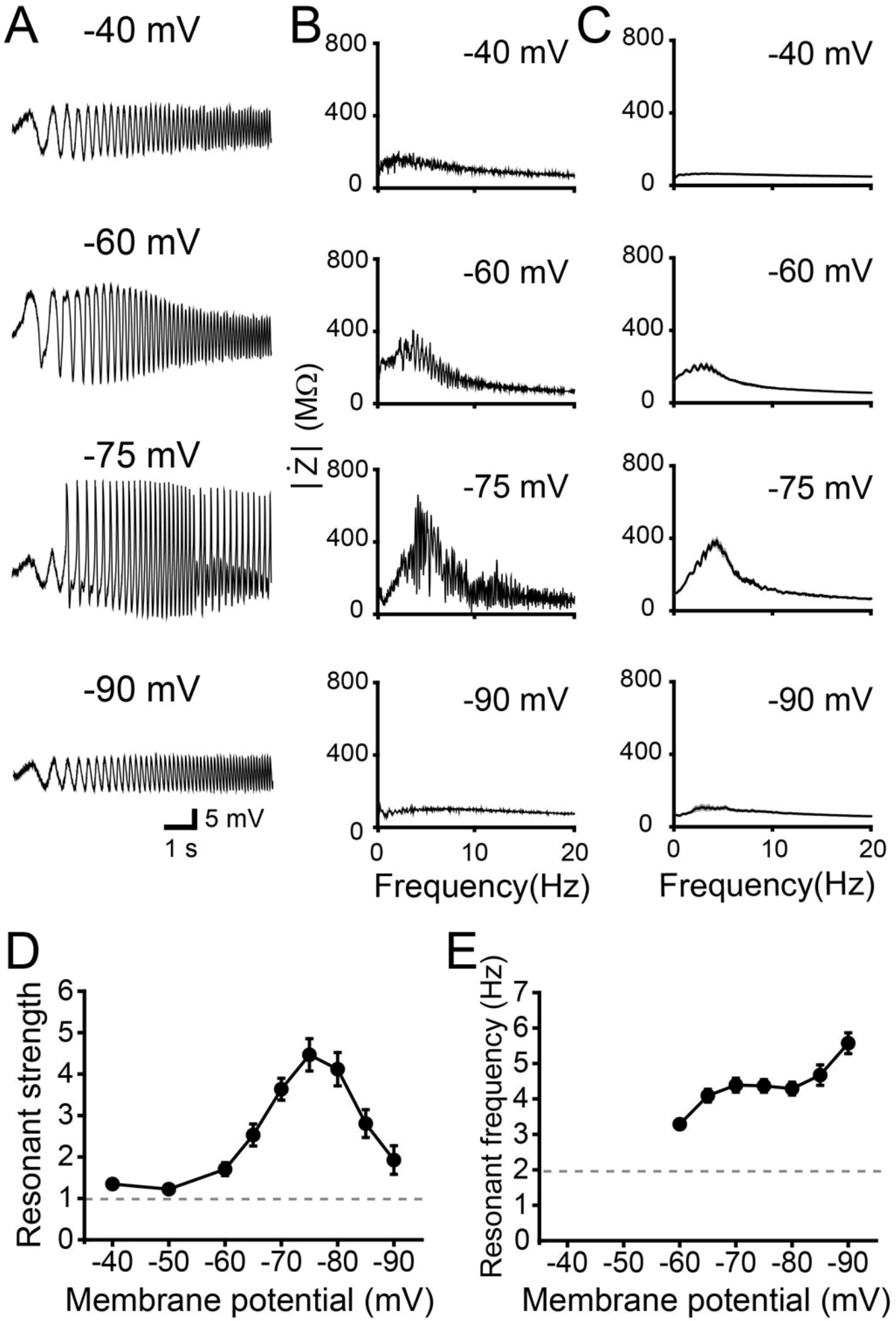
A
-40 mV
-60 mV
-75 mV
-90 mV
5 mV
1 s
B
C
800
400
0
-40 mV
-60 mV
-75 mV
-90 mV
|Ż| (MΩ)
0
10
20
Frequency(Hz)
D
Resonant strength
0
1
2
3
4
5
6
-40 -50 -60 -70 -80 -90
Membrane potential (mV)
E
Resonant frequency (Hz)
0
1
2
3
4
5
6
7
-40 -50 -60 -70 -80 -90
Membrane potential (mV)

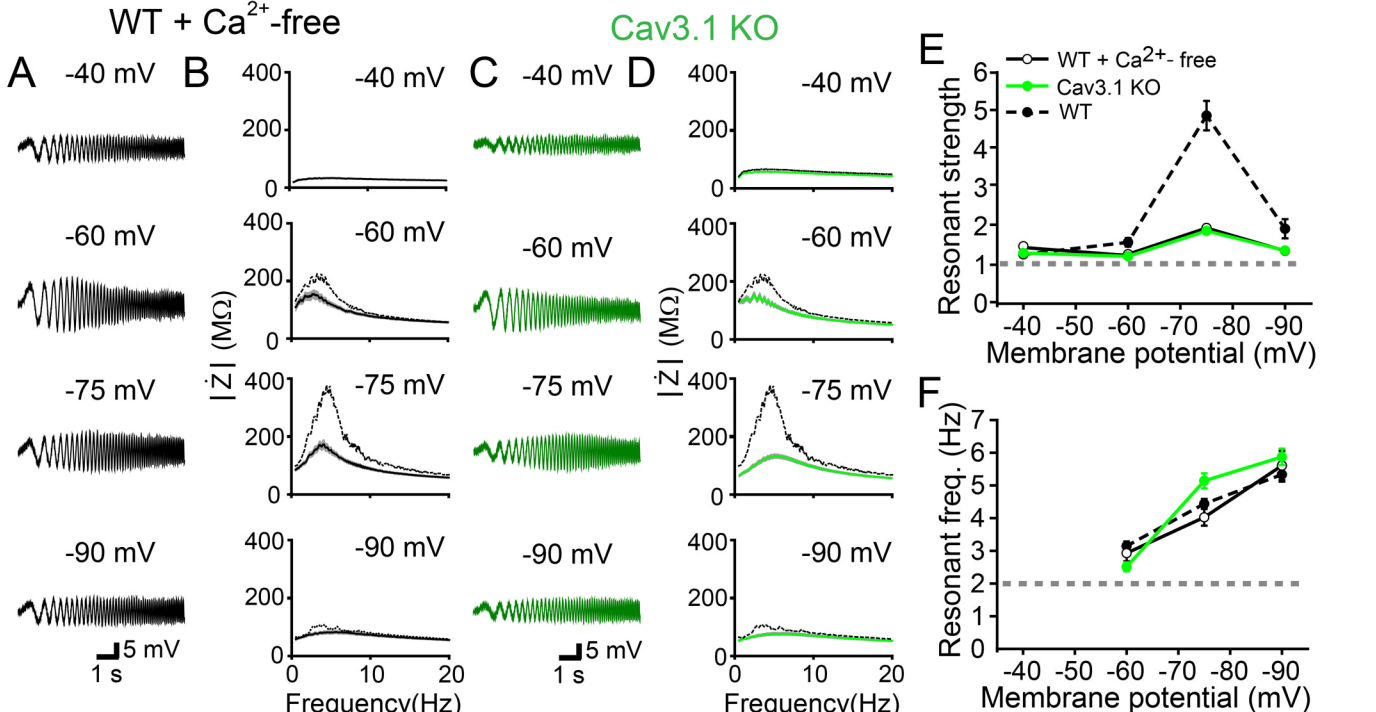
WT + Ca2+-free
Cav3.1 KO
A
B
C
D
E
F
-40 mV
-60 mV
-75 mV
-90 mV
5 mV
1 s
|Ż| (MΩ)
Frequency(Hz)
WT + Ca2+- free
Cav3.1 KO
WT
Resonant strength
Membrane potential (mV)
Resonant freq. (Hz)

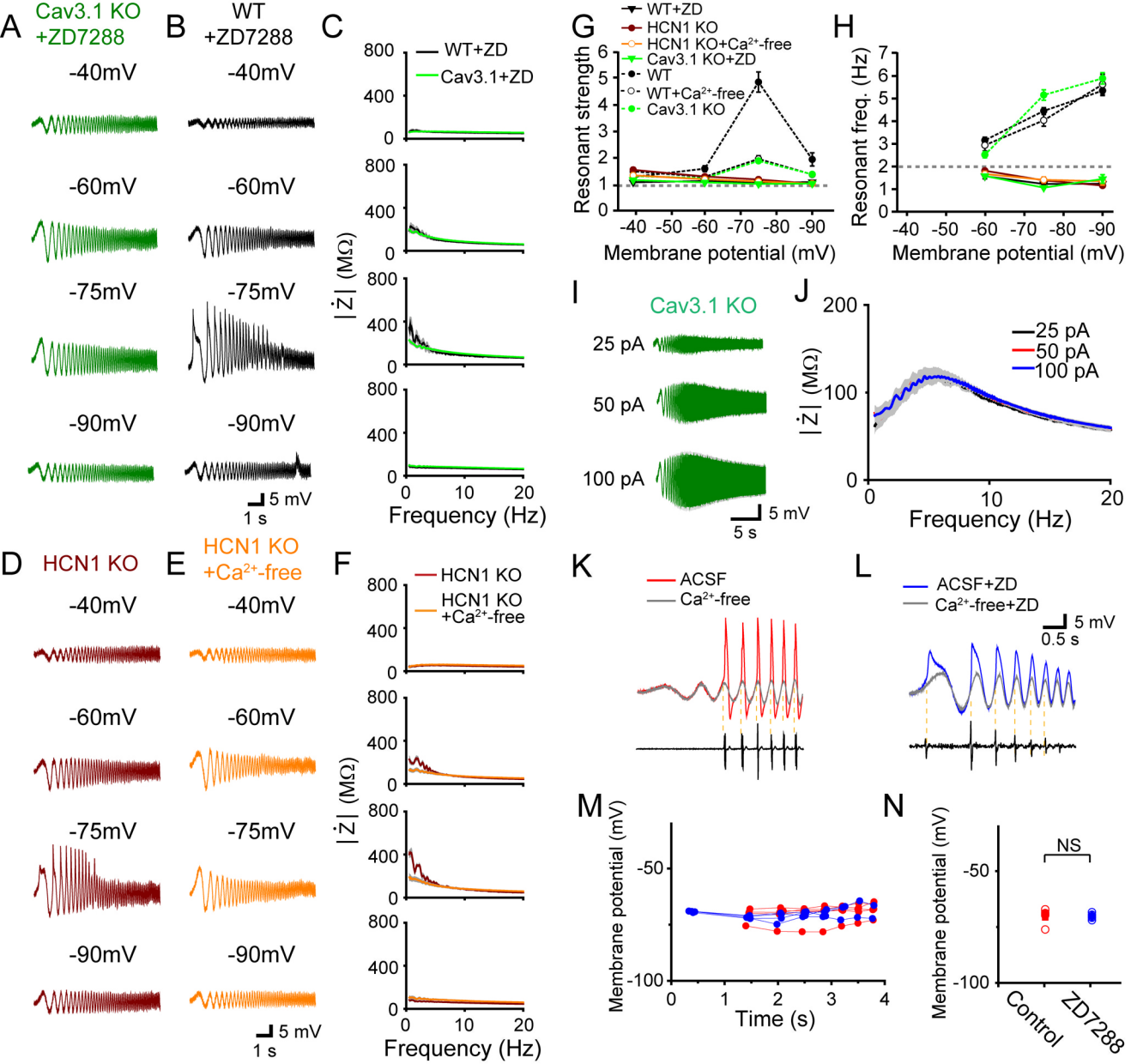
A
Cav3.1 KO
+ZD7288
-40mV
-60mV
-75mV
-90mV
B
WT
+ZD7288
-40mV
-60mV
-75mV
-90mV
5 mV
1 s
C
WT+ZD
Cav3.1+ZD
800
400
0
|Ż| (MΩ)
0
10
20
Frequency (Hz)
D
HCN1 KO
-40mV
-60mV
-75mV
-90mV
E
HCN1 KO
+Ca2+-free
-40mV
-60mV
-75mV
-90mV
5 mV
1 s
F
HCN1 KO
HCN1 KO
+Ca2+-free
800
400
0
|Ż| (MΩ)
0
10
20
Frequency (Hz)
G
WT+ZD
HCN1 KO
HCN1 KO+Ca2+-free
Cav3.1 KO+ZD
WT
WT+Ca2+-free
Cav3.1 KO
Resonant strength
6
5
4
3
2
1
0
-40 -50 -60 -70 -80 -90
Membrane potential (mV)
H
Resonant freq. (Hz)
7
6
5
4
3
2
1
0
-40 -50 -60 -70 -80 -90
Membrane potential (mV)
I
Cav3.1 KO
25 pA
50 pA
100 pA
5 mV
5 s
J
200
100
0
|Ż| (MΩ)
25 pA
50 pA
100 pA
0
10
20
Frequency (Hz)
K
ACSF
Ca2+-free
L
ACSF+ZD
Ca2+-free+ZD
5 mV
0.5 s
M
Membrane potential (mV)
-50
-100
0
1
2
3
4
Time (s)
N
Membrane potential (mV)
-50
-100
NS
Control
ZD7288

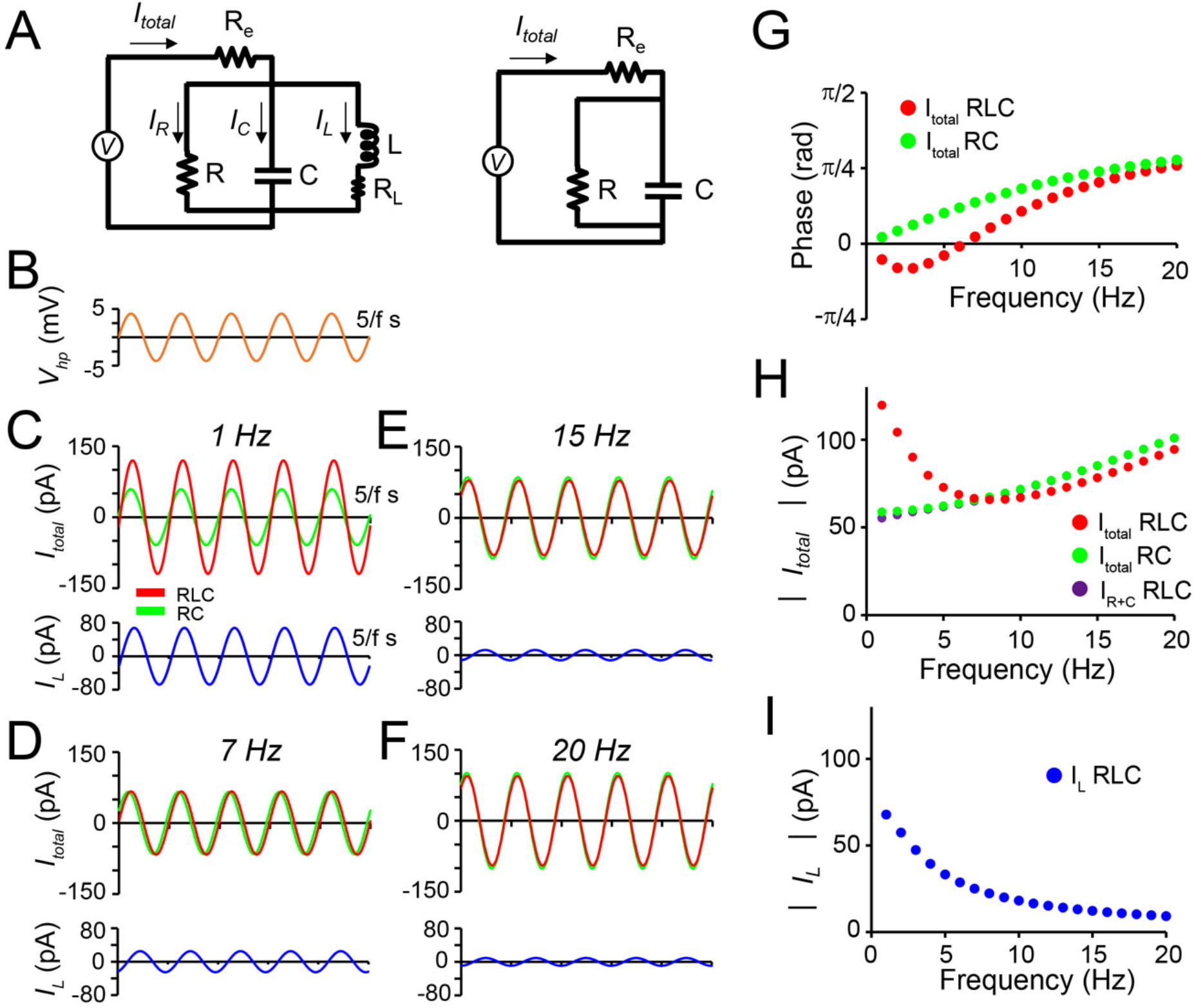
A
$I_{total}$
$R_e$
$I_R$
$I_C$
$I_L$
V
R
C
L
$R_L$
$I_{total}$
$R_e$
V
R
C
B
$V_{hp}$ (mV)
5
-5
5/f s
C
1 Hz
150
0
-150
$I_{total}$ (pA)
5/f s
RLC
RC
80
0
-80
$I_L$ (pA)
5/f s
E
15 Hz
150
0
-150
80
0
-80
D
7 Hz
150
0
-150
$I_{total}$ (pA)
80
0
-80
$I_L$ (pA)
F
20 Hz
150
0
-150
80
0
-80
G
π/2
π/4
0
-π/4
Phase (rad)
$I_{total}$ RLC
$I_{total}$ RC
10
15
20
Frequency (Hz)
H
100
50
0
| $I_{total}$ | (pA)
$I_{total}$ RLC
$I_{total}$ RC
$I_{R+C}$ RLC
0
5
10
15
20
Frequency (Hz)
I
100
50
0
| $I_L$ | (pA)
$I_L$ RLC
0
5
10
15
20
Frequency (Hz)

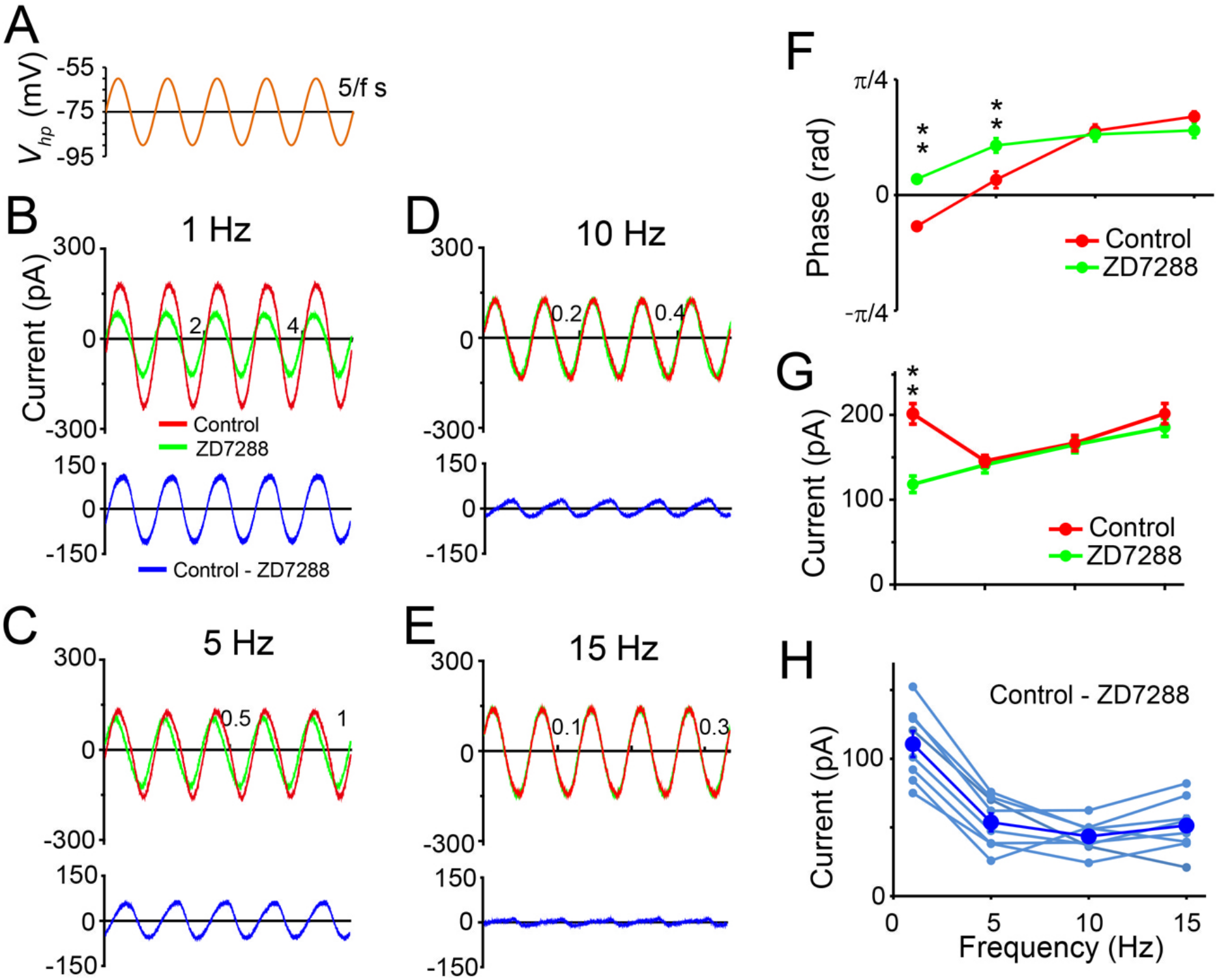
A
$V_{hp}$ (mV)
-55
-75
-95
5/f s
B
1 Hz
Current (pA)
300
0
-300
150
0
-150
2
4
Control
ZD7288
Control - ZD7288
C
5 Hz
0.5
1
D
10 Hz
0.2
0.4
E
15 Hz
0.1
0.3
F
Phase (rad)
π/4
0
-π/4
**
**
Control
ZD7288
G
Current (pA)
200
100
0
**
Control
ZD7288
H
Current (pA)
Control - ZD7288
100
0
0
5
10
15
Frequency (Hz)

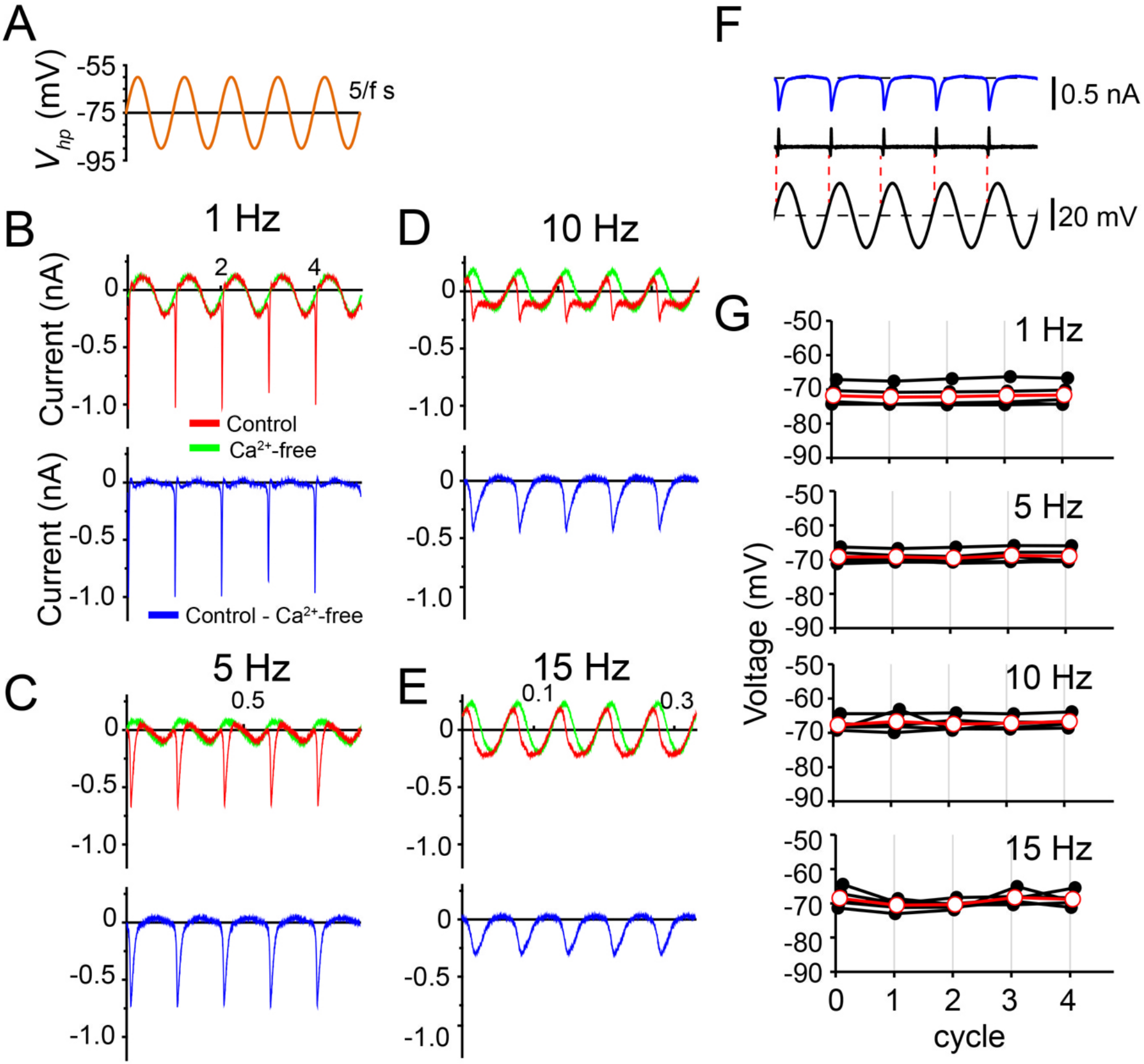
A
$V_{hp}$ (mV)
-55
-75
-95
5/f s
B
1 Hz
2
4
Current (nA)
0
-0.5
-1.0
Control
Ca2+-free
Control - Ca2+-free
C
5 Hz
0.5
D
10 Hz
E
15 Hz
0.1
0.3
F
0.5 nA
20 mV
G
1 Hz
5 Hz
10 Hz
15 Hz
Voltage (mV)
-50
-60
-70
-80
-90
0
1
2
3
4
cycle

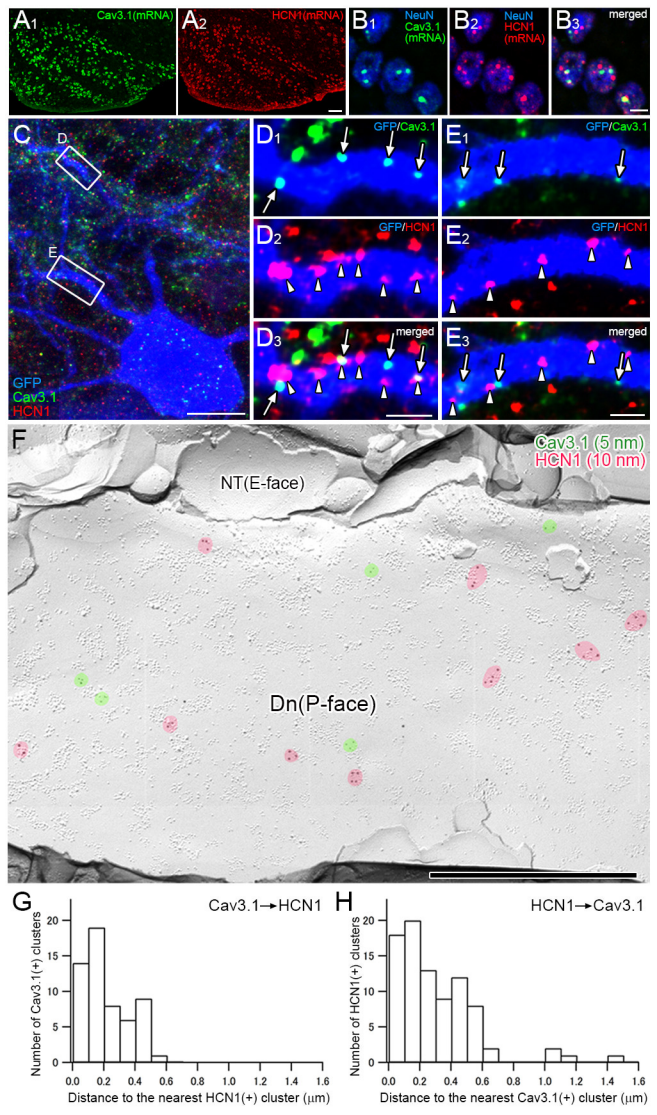
A1
Cav3.1(mRNA)
A2
HCN1(mRNA)
B1
NeuN
Cav3.1
(mRNA)
B2
NeuN
HCN1
(mRNA)
B3
merged
C
D
E
GFP
Cav3.1
HCN1
D1
GFP/Cav3.1
D2
GFP/HCN1
D3
merged
E1
GFP/Cav3.1
E2
GFP/HCN1
E3
merged
F
Cav3.1 (5 nm)
HCN1 (10 nm)
NT(E-face)
Dn(P-face)
G
Cav3.1→HCN1
Number of Cav3.1(+) clusters
Distance to the nearest HCN1(+) cluster (μm)
H
HCN1→Cav3.1
Number of HCN1(+) clusters
Distance to the nearest Cav3.1(+) cluster (μm)

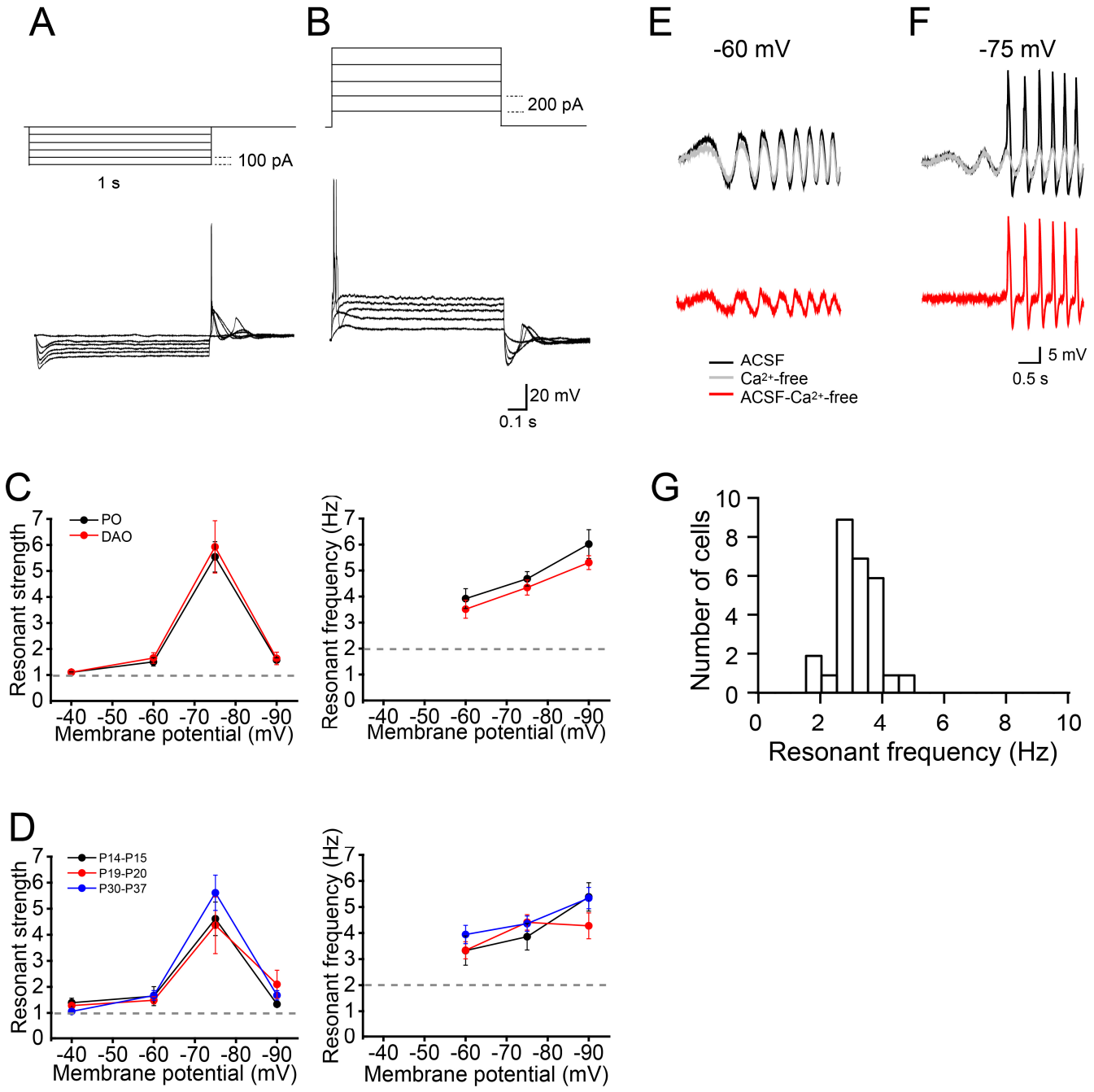


**Figure S1. Physiological properties of IO neurons in WT mice. Related to Figure 1.**

(**A**) Representative voltage traces in response to hyperpolarizing step current injections in a WT IO neuron. The membrane potential was held at −60 mV. Note depolarizing sags at the onset and rebound low threshold $Ca^{2+}$ spikes at the offset of the hyperpolarizing currents. (**B**) Representative voltage traces in response to depolarizing step current injections. (**C**) Membrane potential dependency of resonant strength in the principal olive (PO, black, n = 7) and dorsal accessory olive (DAO, red, n = 7) (left). Membrane potential dependency of the resonant frequency (right). (**D**) Membrane potential dependency of resonant strength at P14–P15 (black, n = 4), P19–P20 (red, n = 6), and P30–P37 (blue n = 9) (left). Membrane potential dependency of resonant frequency (right). (**E, F**) Waveforms of voltage responses recorded in normal (solid) and $Ca^{2+}$-free (gray) external solutions at membrane potentials of −60 (E) and −75 (F) mV. A $Ca^{2+}$-dependent component (red) is isolated by subtracting the voltage response recorded in the $Ca^{2+}$-free external solution (gray) from the voltage response in the normal external solution (black). (**G**) Frequency distribution histogram of resonant frequency at -60 mV near the resting membrane potential. The distribution of resonant frequency is a normal distribution ($p$ = 0.503, Shapiro-Wilk test). Averaged data are presented as mean ± SEM.

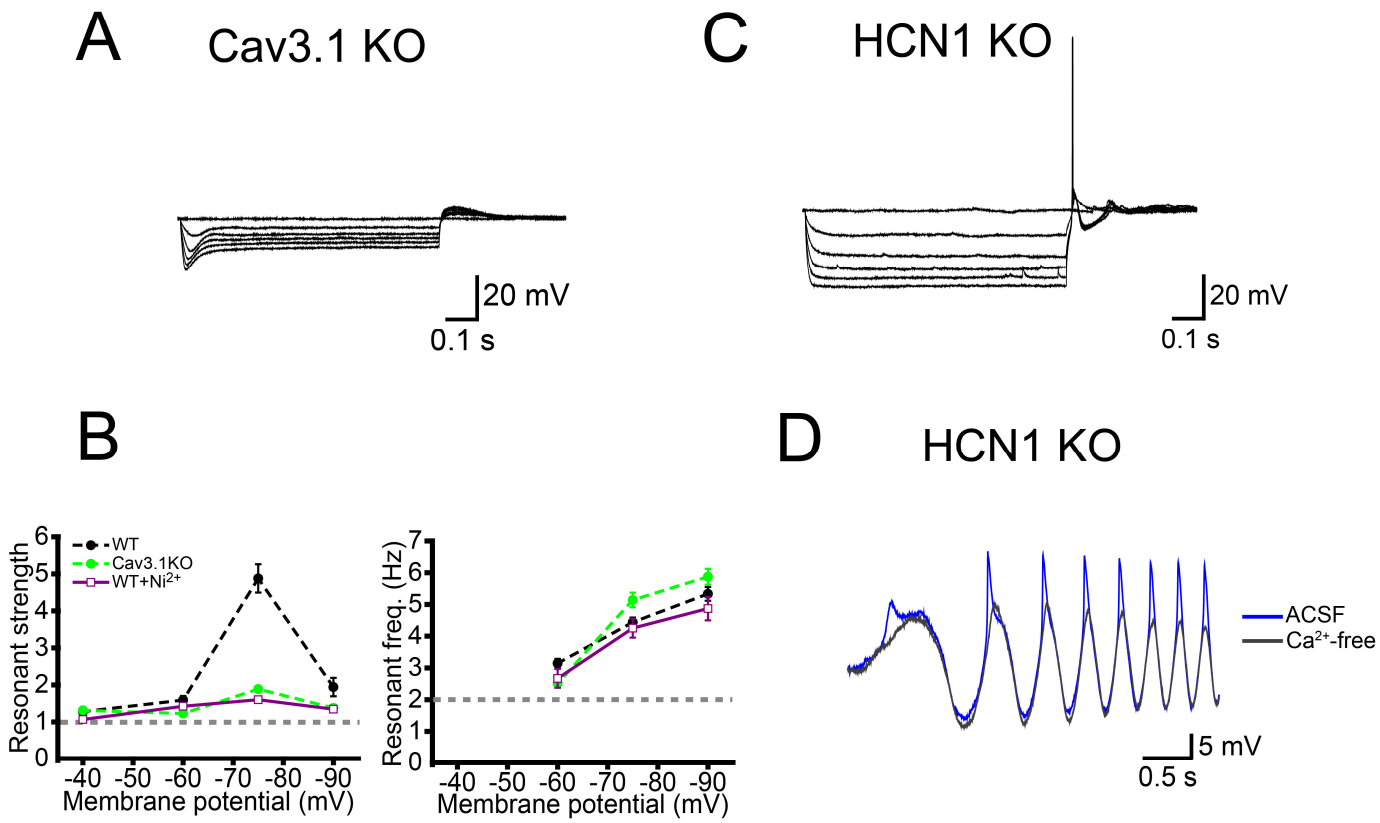


**Figure S2. Electrophysiological properties of IO neurons in Cav3.1 and HCN1 KO mice. Related to Figure 2 and 3.**

(**A**) Representative voltage traces in response to hyperpolarizing current injections in a Cav3.1 KO IO neuron. The membrane potential was held at −60 mV. Generation of the depolarizing sag was normal, but the rebound spike was impaired in Cav3.1 KO mice. (**B**) The effect of $Ni^{2+}$ (200 μM) on resonance in WT mice. Membrane potential dependency of resonant strength (left) and resonant frequency (right). $Ni^{2+}$ strongly suppressed resonance to a level identical to resonance in the Cav3.1 KO mice, but did not alter resonant frequency (n = 8). (**C**) Representative voltage traces in response to hyperpolarizing current injections in an HCN1 KO IO neuron. The membrane potential was held at −60 mV. Note that depolarizing sags were impaired in HCN1 KO mice. (**D**) Waveforms of voltage responses recorded in normal (blue) and $Ca^{2+}$-free (black) external solutions at a membrane potential of −75 mV in an HCN1 KO IO neuron. Similar to traces in Figure 3L, generation of hyperpolarizing potentials of $Ca^{2+}$ spikes is suppressed in HCN1 KO mice. Averaged data are presented as mean ± SEM.

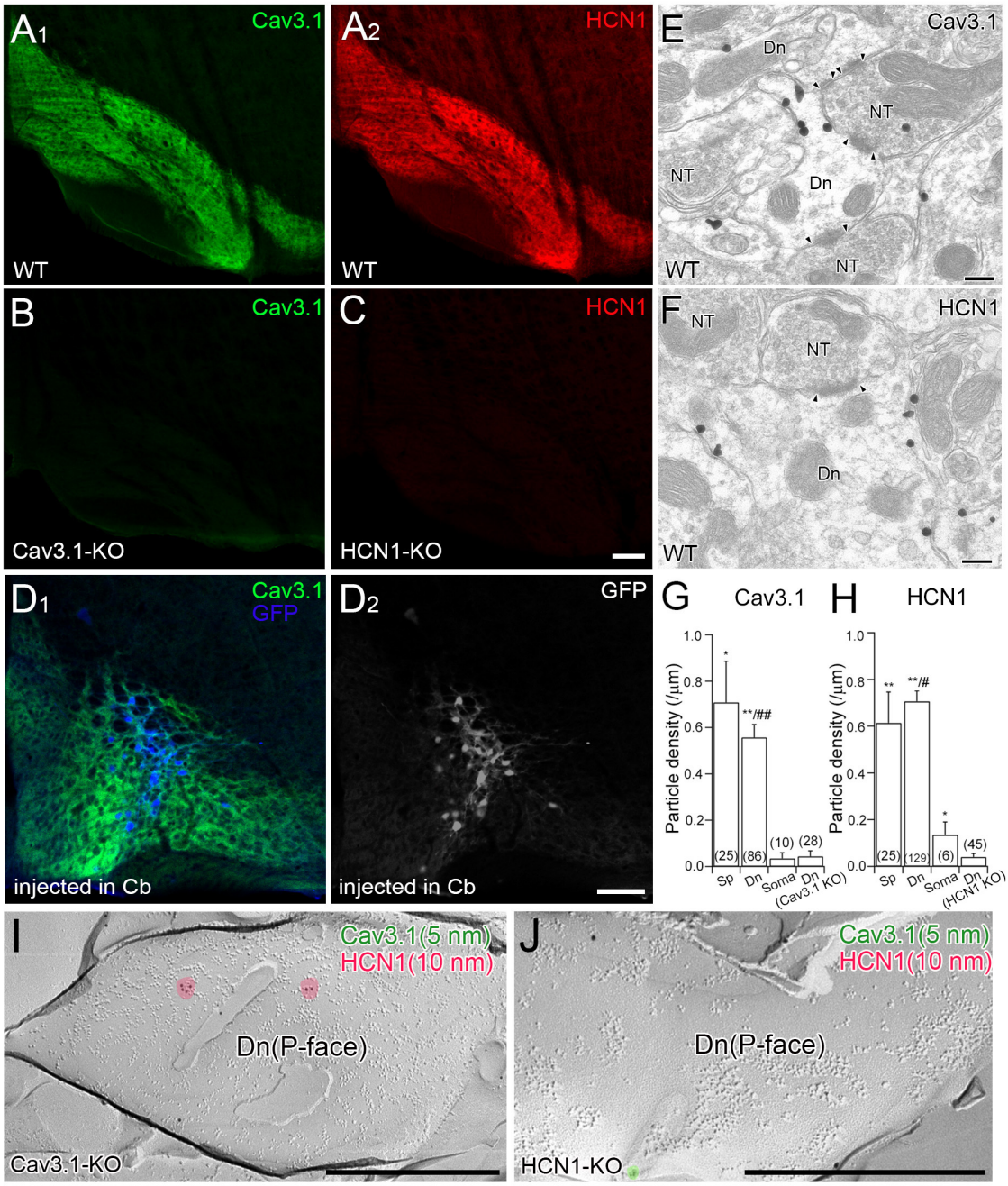


**Figure S3. Specificity of Cav 3.1 and HCN1 antibody and GFP-labeling. Related to Figure 7.**

(**A**) Double immunofluorescence showing prominent Cav3.1 (green) and HCN1 (red) expression in the IO. (**B, C**) Immunofluorescent images showing almost no Cav3.1 or HCN1 expression in corresponding KO mice. Images were obtained at the same acquisition settings in A. (**D**) A small subset of IO neurons were labeled with GFP by a local injection of retrograde lentiviral vector into the cerebellar cortex. (**E, F**) Preembedding immunogold electron microscopy shows that Cav3.1 (E) and HCN1 (F) are preferentially localized on the plasma membrane of IO dendrites. Arrowheads indicate edges of synapses. Dn, dendrite; NT, nerve terminal. (**G, H**) Summary histograms showing density of Cav3.1 (G) and HCN1 (H) particles on dendritic shafts (Dn), spines (Sp), and soma in the WT mice and on dendrites in the KO mice (Dn(KO)). Densities on dendrites and spines in WT mice are significantly higher than dendrite density in KO mice (**$p < 0.01$, *$p < 0.05$; post-hoc Steel-Dwass test). Note that dendritic expression of Cav3.1 and HCN1 is significantly higher than somatic expression (##$p < 0.01$, #$p < 0.05$; post-hoc Steel-Dwass test). The number of measured profiles is indicated in parentheses. Averaged data are presented as mean ± SEM. (**I, J**) SDS-FRL images show that Cav3.1 and HCN1 clusters are not observed in corresponding KO mice. P-face, protoplasmic face. Scale bars, C, D, 100 μm; E, F, 200 nm; I, J, 500 nm.

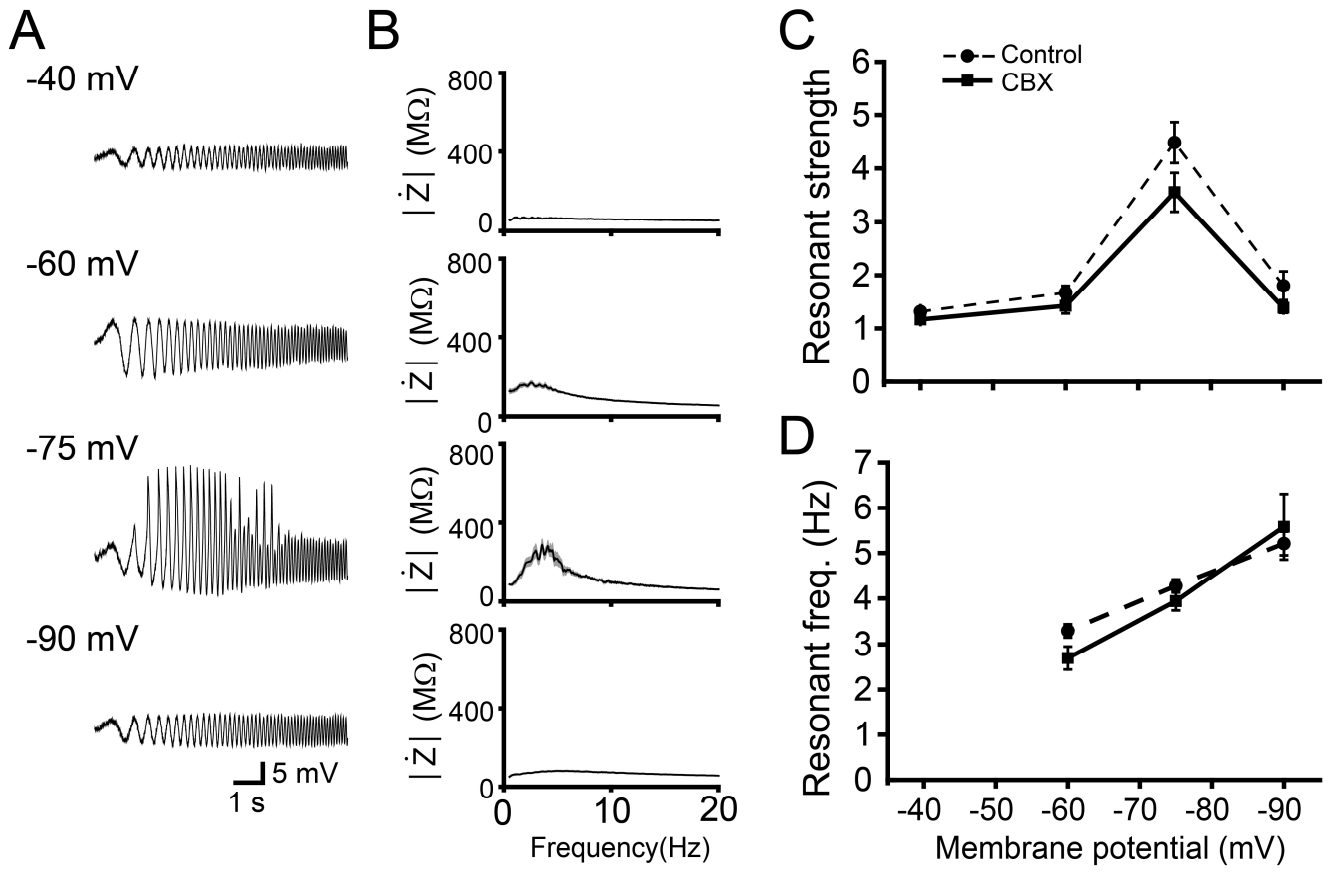


**Figure S4. Effects of carbenoxolone on resonance. Related to Figure 1 and 2.**

(**A**) Representative voltage traces in response to chirp currents (50 pA) in the presence of carbenoxolone (CBX, 100μM), a gap junction blocker, in a WT IO neuron. Input resistance in the presence of CBX (90.8 ± 2.7 MΩ (n = 8)) is significantly larger than in the control external solution (75.4 ± 3.6 MΩ (Table S1), $p$ = 0.007, Mann–Whitney U-test). (**B**) Average *Z-F* profiles (n = 8). Responses were recorded at membrane potentials of –40, –60, –75, and –90 mV. (**C, D**) Membrane potential dependency of resonant strength (C) and resonant frequency (D) in WT IO neurons in the presence of CBX (solid lines) (n = 8). Data for control is the same as WT in Figure 1D, and 1E. Averaged data are presented as mean ± SEM.

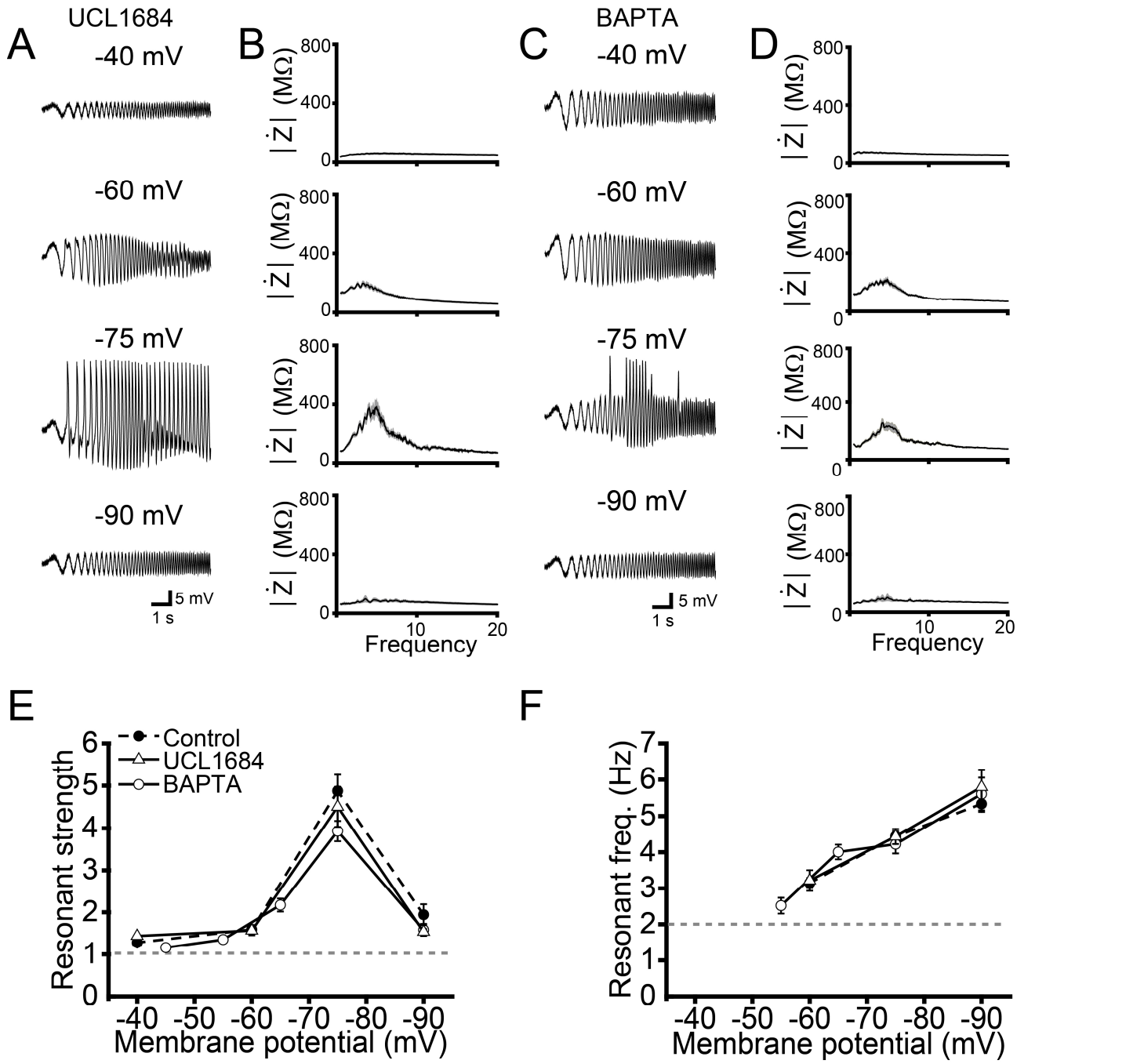


**Figure S5. Roles of $Ca^{2+}$-activated $K^+$ channels in resonance. Related to Figure 1 and 2.**

(**A**) Representative voltage traces in response to chirp current (50 pA) in the presence of UCL1684 (200 nM), a $Ca^{2+}$-activated $K^+$ channel blocker, in a WT IO neuron. Responses were recorded at membrane potentials of –40, –60, –75, and –90 mV. (**B**) Average *Z-F* profiles (n = 8). (**C, D**) Similar to A and B, but data in the presence of intracellular BAPTA (20 mM) in WT mice (n = 15). (**E, F**) Membrane potential dependency of resonant strength (E) and resonant frequency (F) in the presence of UCL1684 (open triangles) or BAPTA (open circles) in WT mice. Data for control is the same as WT in Figure 1D, and 1E. Averaged data are presented as mean ± SEM. The liquid junction potential of intracellular solution with 20 mM BAPTA was adjusted to that of the normal intracellular solution.

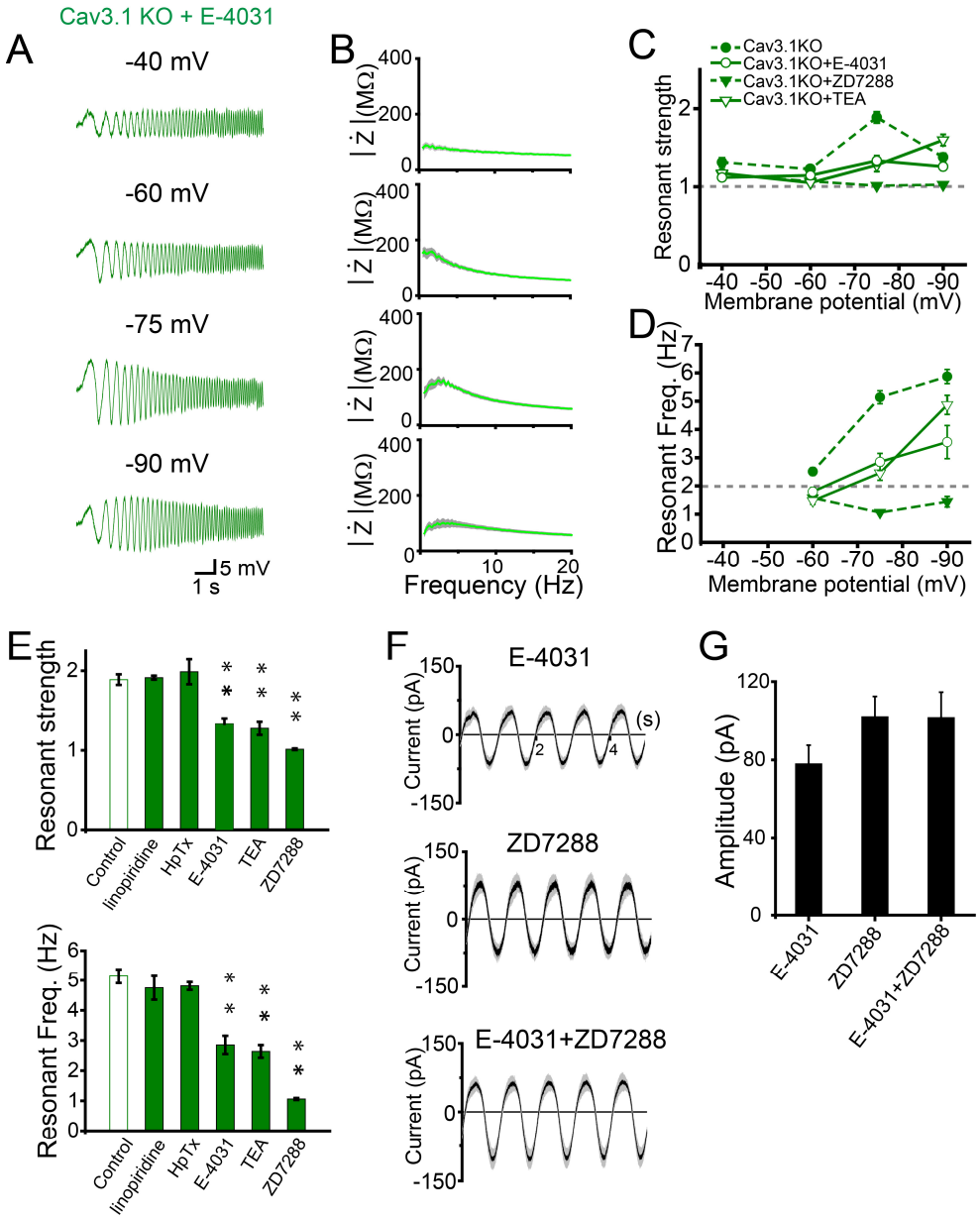


**Figure S6. Voltage-dependent $K^+$ channels modulate ZD7288-sensitive resonance. Related to Figure 3 and 5.**

(**A**) Representative voltage traces in response to chirp current (50 pA) at membrane potentials of −40, −60, −75, and −90 mV in the presence of E-4031 (10 μM) in a Cav3.1 KO IO neuron. (**B**) Average *Z-F* profiles (n = 9). Shaded areas represent mean ± SEM. (**C**) Membrane potential dependency of resonant strength in Cav3.1 KO mice. Data for Cav3.1 KO and Cav3.1 KO + ZD7288 (dotted lines) are the same as those illustrated in Figure 3G. (**D**) Membrane potential dependency of resonant frequency in Cav3.1 KO mice. Data for Cav3.1 KO and Cav3.1 KO + ZD7288 (dotted lines) are the same as those illustrated in Figure 3H. (**E**) Effects of linopiridine (20 μM, n = 3), heteropodatoxin (HpTx, 200 nM, n = 3), E-4031 (10 μM, n = 9), and tetraethylammonium (TEA, applied intracellularly at 5 mM, n = 7) or ZD7288 (n = 11) on resonant strength (upper) and resonant frequency (lower) in Cav3.1 KO mice at a membrane potential of −75 mV. Statistical significance was assessed between control and each blocker (Holm-Sidak test). (**F**) Average traces of E-4031-sensitive (upper), ZD7288-sensitive (middle), and E-4031 + ZD7288 sensitive (lower) currents recorded under the voltage-clamp mode. Currents in response to sinusoidal voltage clamp were measured at −75 mV. Frequency of sinusoidal voltage was 1 Hz, at which the ZD7288-sensitive current was large (Figure 5H). Each current was calculated by subtracting the current recorded in the presence of blockers from that in the normal external solution. (**G**) Averaged amplitudes of E-4031-sensitive, ZD7288-sensitive, and E-4031 + ZD7288 sensitive currents (n = 5). There was no significant difference between groups (one-way ANOVA). Averaged data are presented as mean ± SEM.

| | WT | Cav3.1KO | HCN1KO |
|---|---|---|---|
| **Resting membrane potential (mV)** | –55.2 ± 1.3 (13) | –56.8 ± 1.6 (12) | –61.9 ± 2.5 (10)* |
| **Input resistance (MΩ)** | 75.4 ± 3.6 (13) | 77.6 ± 2.3 (12) | 73.8 ± 7.1 (10) |
| **Firing frequency (Hz)** | 2.7 ± 0.5 (9) | 1.6 ± 0.4 (7) | 1.8 ± 0.5 (8) |
| **Depolarizing sag (mV)** | 16.4 ± 0.6 (13) | 15.4 ± 0.4 (12) | 1.1 ± 0.2 (10)* |
| **Amplitude of rebound spike (mV)** | 27.8 ± 1.1 (17) | 9.2 ± 0.8 (13)* | 19.2 ± 2.2 (9)* |

**Table S1. Electrophysiological properties of IO neurons. Related to Figure 1.**

Data are expressed as mean ± SEM. Number of cells is presented in parentheses. Firing frequency was measured in response to depolarizing pulses with an amplitude of 1 nA. The amplitude of the depolarizing sag was measured from the voltage deflection peak to the steady-state plateau in rebound depolarization during hyperpolarizing pulses with an amplitude of –500 pA. Generation of the depolarizing sag is impaired in HCN1 KO mice. Only the amplitude of rebound spike was measured in the presence of TTX. Amplitude of the rebound spike in WT mice is roughly identical to sum of those in Cav3.1 and HCN1 KO mice. Statistical differences were assessed between WT and KO mice. *$p < 0.05$ (Holm-Sidak test).

**Supplemental Experimental Procedures**

**Slice preparation**

Coronal brain slices, including the inferior olive (IO) (thickness of 250 μm), were prepared from C57BL/6, Cav3.1 KO, and HCN1 KO mice at postnatal days 14–37. Mice were anaesthetized with $CO_2$ gas and subsequently decapitated. A block of the brain containing the medulla was removed and put into the ice-cold cutting solution composed of (mM) 124 sucrose, 10 glucose, 26 $NaHCO_3$, 5 KCl, 1.2 $KH_2PO_4$, 1.3 $MgSO_4$, and 2.4 $CaCl_2$ bubbled with mixed gases (95% $O_2$ and 5% $CO_2$). The medulla block was embedded in 1.5% agarose and sliced using a vibrating blade microtome (VT-1200S, Leica Microsystems).

**Electrophysiology**

Whole-cell recordings were made from neurons in the principal or dorsal accessory olive using an upright microscope (BX51WI; Olympus) equipped with an IR-CCD camera system (IR-1000, DAGE-MTI). Resonance was not significantly different between the IO subnuclei (Figure S1C). In all experiments, the temperature was maintained at 32°C using an inline heater (TC-324B, Warner). An intracellular solution was composed of 115 K-methansulfonate, 5 KCl, 5 NaCl, 0.5 EGTA, 30 HEPES, 4 $MgCl_2$, 4 2Na-ATP, and 0.4 2Na-GTP (in mM) (pH 7.3, adjusted with KOH). The composition of the intracellular solution with BAPTA was 10 K-methansulfonate, 80 KCl, 20 BAPTA-$K_4$, 30 HEPES, 4 $MgCl_2$, 4 2Na-ATP, and 0.4 2Na-GTP (pH 7.3, adjusted with KOH). The pipette access resistance was about 2 to 3 MΩ. Composition of the normal external solution was (in mM): 125 NaCl, 2.5 KCl, 2 $CaCl_2$, 1 $MgSO_4$, 1.25 $NaH_2PO_4$, 26 $NaHCO_3$, and 20 glucose bubbled with 95% $O_2$ and 5% $CO_2$. NBQX (10 μM), (R)-CPP (5 μM), and bicuculline methchloride (10 μM) were added to block synaptic transmission. Tetrodotoxin (TTX, 0.5 μM) was added in the experiments to measure resonance. In the experiments with $Ca^{2+}$-free external solution, $CaCl_2$ was replaced with an equimolar volume of $MgSO_4$. Ionic currents were recorded with an EPC-10 (Heka Elektronik). The signals were filtered at 3 kHz, and digitized at 20 kHz to measure electrophysiological properties of IO neurons or at 1 kHz to analyze resonance. On-line data acquisition and off-line data analysis were performed using PATCHMASTER software (Heka Elektronik). The liquid junction potentials were not adjusted, except in the experiment shown in Figure S5.

**Impedance measurement**

Impedance was measured from non-oscillating neurons as previously described (Hutcheon and Yarom, 2000; Puil et al., 1986). In brief, sinusoidal currents with constant amplitudes, but frequencies that linearly changed from a range of 0 to 40 Hz in 40 s (chirp current), were applied from a recording electrode under the current clamp mode (Lampl and Yarom, 1997; Puil et al., 1986). Magnitude of chirp currents was 50 pA in most experiments, except in Figure 3I and J. Impedance was calculated by dividing the Fast Fourier Transform (FFT) of voltage response by FFT of the chirp current.

$$\dot{Z}(f) = \frac{FFT\ of\ voltage\ response}{FFT\ of\ chirp\ current}$$

$\dot{Z}(f)$ and f represent complex impedance and frequency of input current, respectively. Magnitude of impedance was calculated as follows:

$$\left|\dot{Z}(f)\right| = \sqrt{(Re(\dot{Z}(f))^2 + (Im(\dot{Z}(f))^2}$$

where $Re(\dot{Z}(f))$ and $Im(\dot{Z}(f))$ represent real and imaginary parts of impedance, respectively. The frequency (> 1 Hz) at which impedance reached a maximum was termed 'resonant frequency'. Resonant strength was calculated as the ratio of maximum

impedance amplitude at the resonant frequency relative to impedance amplitude at 1 Hz. These calculations were performed with Igor and Excel. When resonance did not occur or was blocked, impedance monotonically declined with input frequency. In such cases, resonant frequency was equal or near to 1 Hz in the present study. Mean ± SD area in HCN1 KO mice at –60 mV, in which resonance was assumed to be blocked, was 1.63–1.97 Hz. On the other hand, mean ± SD area at –60 mV in WT mice was 2.43–3.87 Hz. We defined that resonance was subtle or did not occur when the resonant frequency was < 2 Hz in the present study.

**Membrane models**

Impedance of the RLC circuit in Figure 4A was expressed in phasor as follows:

$$\dot{Z}_{RLC}(\omega) = R_e + \frac{1}{\frac{1}{R} + j\omega C + \frac{1}{R_L + j\omega L}}$$

$$\dot{Z}_{RC}(\omega) = R_e + \frac{1}{\frac{1}{R} + j\omega C}$$

$\dot{Z}_{RLC}(\omega)$ and $\dot{Z}_{RC}(\omega)$ represent complex impedance of the RLC and RC circuit, respectively. $\omega = 2\pi f$. The output current was calculated as follows:

$$\dot{I}_{RLC}(\omega) = \frac{\dot{V}_{input}(\omega)}{\dot{Z}_{RLC}(\omega)}$$

$$\dot{I}_{RC}(\omega) = \frac{\dot{V}_{input}(\omega)}{\dot{Z}_{RC}(\omega)}$$

$\dot{I}_{RLC}(\omega)$ and $\dot{I}_{RC}(\omega)$ represent complex output currents of the RLC and RC circuit, respectively. $\dot{V}_{input}(\omega)$ is the complex representation of the input voltage:

$$\dot{V}_{input} = V_0 e^{j\omega t}$$

Magnitudes of $\dot{I}_{RLC}(\omega)$ and $\dot{I}_{RC}(\omega)$ were calculated as the magnitude of $\dot{Z}(f)$. The values of parameters were $R$ = 80 MΩ, $C$ = 140 pF, $R_L$ = 60 MΩ, $L$ = 4 MH, and $R_e$ = 5 MΩ. $R$ and $C$ were estimated from voltage traces in response to hyperpolarizing current injections. $R_L$ and $L$ were taken from Narayanan and Johnston (Narayanan and Johnston, 2008).

Absolute amplitudes of the sum of currents flowing in the capacitor and resistance in the RLC circuit ($I_{R+C}$, purple) or in the RC circuit (identical to $I_{total}$ of the RC circuit) slightly deviated at lower frequencies (Figure 4H). This deviation tended to be larger with increase in the series resistance ($R_e$) ($I_{R+C}$ in the RLC and the RC circuits are theoretically identical when $R_e$ = 0) (data not shown), but the difference was small under our recording conditions with relatively low series resistance (3–7 MΩ). In the voltage-clamp experiments, current flowing through the phenomenological inductor was estimated by subtracting current in the presence of blocker (corresponding to RC circuit) from that in control solution (corresponding to RLC circuit).

**Antibodies**

We used the following primary antibodies: guinea pig anti-Cav3.1 (Hildebrand et al., 2009), goat anti-GFP (Takasaki et al., 2010), and rabbit anti-HCN1 (APC-056, Alomone). We also produced an affinity-purified HCN1 antibody, which was raised against amino acid residues 888–910 of mouse HCN1 (NP_034538). The specificity of Cav3.1 and HCN1 antibodies was confirmed by blank immunohistochemical labeling in corresponding KO brains with light and electron microscopic analyses (Figure S3B, C, G, H, I, and J).

**Fluorescent *in situ* hybridization.**

We employed non-isotopic *in situ* hybridization with fluorescein- and digoxigenin (DIG)-labeled cRNA probes for Cav3.1 (nucleotides 2101–3044 bp; GenBank accession number, NM_009783), and HCN1 (414–1047 bp; NM_010408) mRNAs. cRNA probes were synthesized by *in vitro* transcription using the Bluescript II plasmid vector encoding the above cDNAs as previously

described (Yamasaki et al., 2010). Under deep diethyl ether anesthesia, brains were freshly obtained and immediately frozen in powdered dry ice. Frozen sections (20 μm) were cut on a cryostat (CM1900, Leica Microsystems) and mounted on silane-coated glass slides. Digoxigenin (DIG)- or fluorescein-labeled cRNA probes were prepared for simultaneous detection of multiple mRNAs by fluorescent *in situ* hybridization (Yamasaki et al., 2010). In brief, fresh-frozen sections were hybridized with a mixture of DIG- or fluorescein-labeled cRNA probes diluted to 1:500 with hybridization buffer. After stringent post-hybridization washing, DIG and fluorescein were detected using the two-step method as follows: first detection was performed with peroxidase-conjugated anti-fluorescein antibody (Roche Diagnostics, 1:1000, 1.5 h) and the FITC-TSA plus amplification kit (PerkinElmer); second detection was performed with peroxidase-conjugated anti-DIG antibody (Roche Diagnostics, 1:1000, 1.5 h) and the Cy3-TSA plus amplification kit (Perkin Elmer). Residual activities of peroxidase introduced in the first detection were inactivated by incubation with 1.0% $H_2O_2$ for 30 min. After extensive washing and blocking with 10% donkey serum, sections were incubated with 1 μg/mL anti-NeuN antibody (MAB377, Millipore) for 1 h, followed by Alexa647-conjugated anti-mouse IgG (Invitrogen) for 2 h. Images were taken with a laser-scanning microscope (FV1200, Olympus) equipped with 473, 559, and 635 nm diode laser lines and UPlanSApo (20×/0.75) and PlanApoN (60×/1.40 oil immersion) objective lenses (Olympus). All images represent single optical sections. The specificity of each antisense probe was confirmed by its characteristic labeling (Figures 7A and B) and also by blank labeling with the sense probes (data not shown).

**Viral vector preparation and injection.**

For retrograde labeling of IO neurons, lentivirus expressing GFP, a mixture of pCAGkGP1R, pCAG4RTR2, and pCAGGS-FuGB (Kato et al., 2011) vectors, and pCL20c-GFP lentivector plasmids were cotransfected into human embryonic kidney (HEK) 293T cells using the calcium phosphate precipitation method. After 40 h of transfection, culture medium containing virus particles was filtered through 0.22-μm membranes and centrifuged at 27,000 × g for 2 h. Viral particles were finally suspended in PBS (pH 7.2). The lentivirus solution (0.3 μl/site) was injected by air pressure into the vermis of cerebellar lobules 6–7 in wild-type P4 pups under ice-cold anesthesia. After 10 days of survival, mice were anesthetized and fixed by transcardial perfusion with 4% paraformaldehyde in 0.1 M PB (pH 7.2).

**Immunofluorescence**

Under deep pentobarbital anesthesia (100 μg/g body weight, i.p.), wild-type P15 mice were fixed transcardially with 4% paraformaldehyde in 0.1 M PB (pH 7.2). After 4-h post-fixation in the same fixative, coronal sections (50 μm thick) were cut with a microslicer (VT1000S, Leica Microsystems). The following incubations were performed at room temperature (25°C). Sections were incubated with 10% normal donkey serum for 20 min, followed by a mixture of primary antibodies (1 μg/mL each) overnight and a mixture of Alexa Fluor 488-, Alexa Fluor 647-(Invitrogen) and Cy3-conjugated (Jackson Immunoresearch) species-specific secondary antibodies for 2 h at a dilution of 1:200. Images were taken with a laser-scanning microscope (FV1200, Olympus) using a PlanApoN (60×/1.40 oil immersion) objective lens (Olympus). To avoid cross-talk between multiple fluorophores, fluorescent signals were sequentially acquired using individual excitation laser lines with a 3× digital zoom and an appropriated pinhole (120 μm). Images were digitized at 12-bit resolution into an array of 800 × 800 pixels (pixel size, 0.1 μm).

**Preembedding immunogold electron microscopy.**

Under deep pentobarbital anesthesia (100 μg/g body weight, i.p.), P15 mice were transcardially fixed with 4% paraformaldehyde, 15 v/v% picric acid, and 0.05% glutaraldehyde in 0.1 M PB (pH 7.2) for 10 min. After 4-h post-fixation in the same fixative, coronal sections (50 μm thick) were cut with a microslicer (VT1000S, Leica Microsystems). Afterwards, the sections were incubated in goat Blocking Solution (Aurion) for 30 min and incubated overnight with primary antibodies (1 μg/mL) diluted with 1% BSA/0.002% saponin/PBS, followed by secondary antibodies linked to 1.4-nm gold particles (Nanogold,

Nanoprobes) for 4 h. Immunogolds were intensified with a silver enhancement kit (R-GENT SE-EM, Aurion). Sections were treated with 1% osmium tetroxide for 15 min, stained in blocking solution with 2% uranyl acetate for 15 min, dehydrated, and embedded in Epon 812. Photographs were taken with an electron microscope (H-7100, Hitachi). For quantitative analysis, plasma membrane-associated immunogold particles, defined as < 30 nm apart from cell membrane, were quantified on electron micrographs and analyzed using MetaMorph software (Molecular Devices). For four-group comparison, Kruskal-Wallis test with the post-hoc Steel-Dwass multiple comparison procedure was performed.

**SDS-digested freeze-fracture replica labeling**

SDS-FRL was performed with some modifications (Indriati et al., 2013) of a previously developed technique by Fujimoto (Fujimoto, 1995). Under deep pentobarbital anesthesia (100 μg/g body weight, i.p.), WT, Cav3.1 KO, and HCN1 KO P15 mice were perfused by 2% PFA in 0.1 M PB (pH 7.2) for 10 min and coronal sections were prepared (150 μm thick). A small region containing the IO was trimmed, and sections were immersed in graded glycerol of 10–30% in 0.1 M PB at 4°C overnight, and then rapidly frozen by a high-pressure freezing machine (HPM010, Leica Microsystems). Frozen samples were fractured into two parts at −140°C and replicated by carbon deposition (2 nm thick), platinum (unidirection from 60°, 2 nm), and carbon (15 nm) in a freeze-fracture replica machine (JFD II, JEOL). Tissue debris was dissolved with gentle shaking at 80°C for 18 h in a solution containing 15 mM Tris-HCl (pH 8.3), 20% sucrose, and 2.5% SDS. The replicas were washed in graded polyethylene glycol (PEG) of 0.5–5% in washing buffer [50 mM Tris-buffered saline (TBS), pH 7.4, containing 0.05% bovine serum albumin (BSA)] and blocked with 5% BSA and 0.5% PEG in washing buffer for 1 h at room temperature. The replicas were then incubated with rabbit anti-HCN1 antibody (Alomone; 2 μg/ml) overnight at 15°C, followed by incubation with species-specific gold particle-conjugated secondary antibody (5 nm, BBI) overnight at 15°C. After extensive washing, the replicas were incubated with guinea pig anti-Cav3.1 antibody (5 μg/ml) overnight at 15°C and species-specific gold particle-conjugated secondary antibody (15 nm, BBI) overnight at 15°C. After immunogold labeling, the replicas were rinsed three times with 0.05% BSA/TBS, washed with TBS and distilled water, and placed onto grids coated with formvar. Images were taken with an electron microscope (JEM 1400, JEOL). Image analysis, including quantification of the number of gold particles and measuring distance of nearest neighbor distance between Cav3.1 and HCN1 clusters, was conducted using MetaMorph software (Molecular Devices).

**Drugs**

Bicuculline, (R)-CPP, NBQX, ZD7288, UCL1684, E-4031 dihydrochloride, and linopiridine dihydrochloride were obtained from Tocris Bioscience. Heteropodatoxin-2 was obtained from Alomone Lab. BAPTA was obtained from Thermo Fisher Scientific. Carbenoxolone was obtained from Sigma Aldrich. Tetrodotoxin and tetraethylammonium chloride were obtained from Nacalai Tesque (Japan).

**Supplemental References**

Fujimoto, K. (1995). Freeze-fracture replica electron microscopy combined with SDS digestion for cytochemical labeling of integral membrane proteins. Application to the immunogold labeling of intercellular junctional complexes. J. Cell Sci. *108* (Pt 11), 3443–3449.

Indriati, D.W., Kamasawa, N., Matsui, K., Meredith, A.L., Watanabe, M., and Shigemoto, R. (2013). Quantitative localization of Cav2.1 (P/Q-type) voltage-dependent calcium channels in Purkinje cells: somatodendritic gradient and distinct somatic coclustering with calcium-activated potassium channels. J. Neurosci. *33*, 3668–3678.

Kato, S., Kuramochi, M., Kobayashi, K., Fukabori, R., Okada, K., Uchigashima, M., Watanabe, M., Tsutsui, Y., and Kobayashi, K. (2011). Selective neural pathway targeting reveals key roles of thalamostriatal projection in the control of visual discrimination. J. Neurosci. *31*, 17169–17179.

Yamasaki, M., Matsui, M., and Watanabe, M. (2010). Preferential localization of muscarinic M1 receptor on dendritic shaft and spine of cortical pyramidal cells and its anatomical evidence for volume transmission. J. Neurosci. *30*, 4408–4418.